Irradiation-Induced Processes with Atomic Clusters and Nanoparticles

Alexey Verkhovtsev, Andrei V. Korol and Andrey V. Solov'yov

Abstract This chapter gives an overview of theoretical and computational studies of physical phenomena manifesting themselves in photon, electron and ion collisions with atomic clusters and nanoparticles (NPs). The emphasis is made on ion and electron scattering as well as photoabsorption of metal NPs which are of current interest in application in cancer treatments with ionizing radiation. Although the number of reports on dose enhancement and radiosensitization due to metal NPs has been rapidly increasing during the past years, physical mechanisms of enhanced production of secondary electrons and reactive species due to sensitizing NPs are still a debated issue and require thorough investigation. In this chapter, we elucidate the essential role of collective electron excitations in the formation of electron emission spectra of metal clusters and NPs. These effects appear also in other types of nanoscale systems, such as carbon-based NPs. We also briefly overview a number of recent Monte Carlo-based studies devoted to the investigation of radiosensitization and dose enhancement effects for proton irradiation combined with metal NPs.

A. Verkhovtsev (✉)
Instituto de Fisica Fundamental, Consejo Superior de Investigaciones Cientificas (CSIC),
Serrano 113-bis, 28006 Madrid, Spain
e-mail: verkhovtsev@iff.csic.es

A. Verkhovtsev · A.V. Korol
MBN Research Center,
60438 Frankfurt am Main, Germany
e-mail: korol@th.physik.uni-frankfurt.de

A.V. Korol
Department of Physics, St. Petersburg State Maritime Technical University,
Leninskii Prospekt 101, 198262 St. Petersburg, Russia

A.V. Solov'yov
MBN Research Center at Frankfurter Innovationszentrum Biotechnologie,
Altenhöferallee 3, 60438 Frankfurt am Main, Germany
e-mail: solovyov@mbnresearch.com

A.V. Solov'yov
A.F. Ioffe Physical-Technical Institute, Polytekhnicheskaya Ul. 26,
194021 Saint Petersburg, Russia

A.V. Solov'yov (ed.), *Nanoscale Insights into Ion-Beam Cancer Therapy*,
DOI 10.1007/978-3-319-43030-0_7

1 Introduction

At present, there is a vivid scientific interest in studying the interaction of nanoscale systems, such as atomic clusters and nanoparticles (NPs), with biological media because of the large number of possible applications in nanomedicine [1, 2]. One of the promising ideas is the use of metal-based NPs or small atomic clusters in cancer treatments with ionizing radiation [3–8]. It has been suggested that such NPs, being delivered to the tumor region, can act as radiosensitizers. They may locally enhance the radiation damage of the tumor cells relative to normal tissues thereby increasing the efficiency of treatments with ionizing radiation. Understanding and exploiting the nanoscale processes that drive physical, chemical, and biological effects induced by ionizing radiation in combination with radiosensitizing NPs is within the scope of an ongoing international project, entitled "Advanced Radiotherapy, Generated by Exploiting Nanoprocesses and Technologies (ARGENT)", supported by the European Commission [9]. Activities undertaken within this project are described in more detail in Chap. 12 of this book.

Currently investigated NPs are generally composed of metals or metal-based materials that can strongly absorb and re-emit radiation energy, resulting in a local radiation dose increase when they are accumulated in tumors [10–12]. Such nanoagents delivered to the tumor region can boost the production of secondary electrons, free radicals, and other reactive species [13–15], which are formed as a result of energy deposition by ionizing radiation in a biological medium [16, 17]. Of particular research interest is the production of low-energy electrons which have the kinetic energy from a few electronvolts to several tens of electronvolts. It is currently established that the secondary electrons of such low energies play an important role in the nanoscale mechanisms of biological damage resulting from ionizing radiation [18, 19].

After the first experimental evidence of radiosensitization by gold NPs [4], a number of follow-up experiments with platinum, silver and gadolinium-based NPs [20–24] demonstrated an increase of cancer cell killing during the X-ray irradiation. Several experiments were performed also with the combination of NPs and ion beams [5, 25–27]. Experiments performed at the molecular scale (using plasmid DNA as a probe) have shown that the addition of platinum NPs during irradiation with C^{6+} and He^{2+} ions amplifies the induction of important DNA lesions, such as double strand breaks [5]. Very recently, similar effects were also observed with small platinum and gadolinium-based NPs irradiated with protons [28].

Despite an increased number of studies on radiosensitization effects of metal NPs, the physical mechanisms of an enhanced yield of secondary electrons emitted from these nanoagents and the subsequent enhancement of the reactive species production are still not entirely understood. For photon beams, the effects of gold NPs have been explained recently by microscopic mechanisms [6], however it is still not established whether similar mechanisms play the main role in the irradiation with ions. This chapter gives an overview of theoretical studies of physical phenomena manifesting themselves in photon, electron and ion collisions with atomic clusters and NPs. We emphasize the essential role of collective electron excitations in strong electron emission from these systems. In particular, we describe recent theoretical and computational studies of the physical mechanisms of the enhanced production of secondary electrons from sensitizing NPs under ionizing irradiation. We describe recent achievements in the analysis of electron production by NPs under ion impact, while irradiation with photons is also briefly discussed. The main focus is made on gold, platinum, silver and gadolinium NPs, which are of current interest [5–7, 22, 25] for radiotherapy applications.

2 Monte Carlo Simulations of Dose Enhancement and Radiosensitization Due to Nanoparticles

Several hypotheses have been proposed recently to understand microscopic mechanisms of radiosensitization by gold NPs irradiated with X-rays. Monte Carlo simulations revealed that the nanoscale dose distribution around gold NPs is highly non-uniform, so that very high doses are deposited in the nearest region around the NP. The dose enhancement (i.e., the increase in energy deposited in the target volume) on the nanoscale was explained by the large number of Auger electrons produced following ionization in the elements with large atomic number [6, 11, 29]. A similar explanation was also given for nanoscale effects arising in the presence of gadolinium-based NPs irradiated with X-rays [30]. It was stated that Auger electrons deposit locally their energy in a region of up to a few tens of nanometers around the NP, leading to highly localized nanoscale doses.

Despite extensive research on NP sensitization under photon irradiation, much smaller number of theoretical and computational studies have been carried out for ion beams. Ion-beam cancer therapy (IBCT) is currently considered as one of the most promising modern treatment techniques [16, 31, 32] because it allows one to deliver a higher dose to the target region, as compared to conventional radiotherapy with X-rays, and also to minimize the exposure of healthy tissue to radiation [32]. Very recently, several Monte Carlo-based studies have evaluated the local dose enhancement for proton irradiation combined with metal NPs [33–36]. The first study of this kind was presented in Ref. [33] where electron emission from 4 and 44 nm NPs composed of gold, platinum, silver, gadolinium, and iron, was investigated by means of the track structure Monte Carlo code TRAX [37]. In the simulations, the NPs were irradiated with 2, 80 and 300 MeV monoenergetic proton beams. A data set of elastic and inelastic (direct ionization, production of Auger electrons, and excitations) cross sections was used in order to track low-energy electrons in the target materials down to energies of a few eV. The simulations demonstrated that the maximal dose enhancement is achieved in the case of platinum and gold NPs, being in the range from 1.9 to 2.5 depending on the NP size. The estimated range of the excess dose was about 5 nm from the surface of small NPs and about 20 nm from the large ones. It was stated that Auger electrons and Auger cascades make a significant contribution to the observed dose enhancement on a nanoscopic level.

In Ref. [34], Monte Carlo simulations were performed to compare the sensitization effect of a 50 nm gold NP using photon and proton beams. The simulations were carried out using the TOPAS (TOol for PArticle Simulation) tool [38]. It was demonstrated that the mechanism by which gold NPs can lead to dose enhancement is different in the case of photon and proton irradiation. For instance, it was shown that for the same amount of energy absorbed inside the NP the difference in the doses deposited by secondary electrons within several nanometers from the NP surface does not exceed 20 % for different radiation sources. However, secondary electrons produced by kilovoltage photons cause a dose enhancement an order of magnitude higher than that caused by protons 10 μm away from the NP surface. Thus, it was concluded that the sensitization effect is radiation type dependent, so that proton therapy can only be enhanced if the NPs and located in close proximity to the biological target being effectively internalized in the cells.

In the subsequent work [35] performed by the same group, the authors adopted the similar methodology to study biological effects of gold NPs radiosensitization, depending on their size and localization inside a cell. The simulations were performed for the NPs ranging from 2 to 50 nm in diameter. For the same mass of gold NPs in the cells, the maximal sensitization effect was observed for smaller systems. This was explained by a higher fraction of low-energy electrons escaping from the 2 nm NPs and thus contributing to the local dose enhancement. As a result of the simulations, it was also concluded that proton radiotherapy can be significantly enhanced with gold NPs only if these nanoagents are internalized into cells. Because of the shorter range of secondary electrons generated by protons, as compared to kilovoltage photons [34], gold NPs cannot contribute to direct DNA damage being located in the extracellular medium. Thus, the cellular uptake is crucial to bring NPs in close proximity to the cell nucleus.

In Ref. [36], Monte Carlo simulations were performed to assess the NP-induced dose enhancement under proton irradiation for several conditions, including several NP types and sizes (gold and gadolinium NPs with 4 and 50 nm in diameter), various distances between the radiation source and the NP, and various source sizes. The simulation results demonstrated that the number of electrons produced by a gold NP is 2–3 times higher than that emitted from a Gd NP of the same size and exceeds by an order of magnitude that emitted from equivalent volume of water. The contribution of Auger electrons to the obtained dose distributions was found to be insignificant (around 1 % at a few nm distance from the NP surface), that agreed with the results of Ref. [34] but contradicted with the results of Ref. [33]. This discrepancy was explained by diverse physical models used in different simulations. The calculated dose enhancement ratio was equal to 1.4–1.7 for gold and 1.1–1.2 for gadolinium, depending on the NP size and geometry of the simulation. As a result of this study, it was concluded that more realistic configurations (i.e., when the proton source is located not at the NP surface but at some distance from it) lead to a very small increase in dose deposition that is mostly located within 1–3 nm from the NP surface.

Most of the above described simulations have been carried out using a 'Geant4-Penelope' physics model for metals, which tracks electrons down to the energy of 100 eV [39]. A similar cutoff exists in other models for tracking low-energy electromagnetic interactions in Geant4 [39]. Thus, the simulation of secondary electron production from metal NPs by means of this approach is limited to the electrons with kinetic energy greater than 100 eV. Microdosimetry models included into the 'Geant4-DNA' physics package allow one to analyze the ionization and excitation spectra in water down to 7.4 eV but are not adapted for studying the production of low-energy secondary electrons in metal materials. Because of a lack of an accurate description of low-energy electrons in most of Monte Carlo simulations, many important physical processes involving these particles may be missing, and it may affect directly the outcome of the simulations. Important phenomena which are not accounted for in most of such simulations is the formation and decay of collective electron excitations which play a significant role in the ionization and excitation of metallic systems. These phenomena are addressed in detail further in this chapter.

3 Collective Electron Excitations in Metal Clusters and Nanoparticles

Metallic clusters and NPs are characterized by a full delocalization of their valence electrons. To some extent this feature is also valid for carbon fullerenes and polycyclic aromatic hydrocarbons (PAHs), where the delocalization of electrons takes place within aromatic rings. Due to the presence of highly mobile delocalized valence electrons, all these systems are highly polarizable. Collective oscillations of delocalized electrons can be excited by a photon or a charged projectile (e.g., an electron or an ion). Such collective excitations are known as plasmons [40, 41].

When considering electron, photon and ion collisions with metal clusters and NPs as well as fullerenes, the delocalized valence electrons often play the most important role in the formation of the cross sections of various collision processes. Plasmon excitations appear as prominent resonances in the cross sections, and the position of the resonance peak depends strongly on the type of a system [42–45]. Investigation of electron collisions with metal clusters and fullerenes in a gas phase has led to manifestation of the interference and diffraction phenomena [46–51], the role of surface and volume plasmon excitations in the formation of electron energy loss spectra [48–54], as well as the total inelastic scattering [48, 49], photoabsorption [55] and photoionization cross sections [56, 57]. All these phenomena are described below in this section.

3.1 Diffraction of Fast Electrons on Atomic Clusters

The phenomenon of elastic scattering of fast electrons on metal clusters and fullerenes appears because the ionic density distribution in a cluster is typically characterized by a rigid border. The presence of a surface in a cluster results in the specific oscillatory behavior of the electron elastic scattering cross sections, which can be interpreted in terms of electron diffraction by the cluster surface [48, 51]. The detailed theoretical treatment of the diffraction phenomena arising in electron scattering on metal clusters and fullerenes was given in Refs. [48–50]. Experimentally, diffraction in electron elastic scattering cross sections on gas-phase fullerenes was observed for the first time in Ref. [51].

Let us explain the physical nature of the diffraction phenomena arising in elastic electron–cluster scattering. For the sake of simplicity, we consider atomic clusters as spherically symmetric systems with a uniform electron density distribution; this model is well applicable, e.g., to highly-symmetric 'magic'-number metal clusters or carbon fullerenes. The cross section of elastic scattering of a fast electron on a cluster in the first Born approximation (see, e.g., Ref. [58]) reads as (in this chapter we use the atomic system of units, $m_e = |e| = \hbar = 1$):

$$\frac{d\sigma}{d\Omega_{\mathbf{p}_2}} = \frac{4}{q^4} F(q)^2 \, . \tag{1}$$

Here, $F(q)$ is the form-factor of the cluster, $q = |\mathbf{p}_2 - \mathbf{p}_1|$ is the momentum transfer, with $\mathbf{p}_1$, $\mathbf{p}_2$ being the momenta of the electron in the initial and the final state, respectively, and $d\Omega_{\mathbf{p}_2}$ denotes the differentiation over the solid angle of the scattered electron. The magnitude of q^2 is related to the scattering angle $\theta = \widehat{\mathbf{p}_1 \, \mathbf{p}_2} \ll 1$ rad via:

$$q^2 = p_1^2 + p_2^2 - 2p_1p_2\cos\theta = 2p_1^2(1-\cos\theta) \approx p_1^2\theta^2 \, . \tag{2}$$

The form factor of the target, $F(q)$, can be expressed as product of the form factor of the atomic concentration, $n(q)$, and the form factor of a single atom, $F_A(q)$:

$$F(q) = F_A(q) \sum_j e^{i\mathbf{q}\mathbf{r}_j} = F_A(q)\, n(q) \tag{3}$$

where the summation is performed over all coordinates, $\mathbf{r}_j$, of all atoms in the cluster. The applicability of this approximation has been examined in Ref. [51] for metal clusters and fullerenes.

The form factor of the atomic concentration, $n(q)$, depends on the geometry of the cluster. In the case of the *metal cluster*, assuming a homogeneous distribution of atoms in the volume of the cluster of the radius R, one derives

$$n(q) = 3N \left[\frac{\sin(qR)}{(qR)^3} - \frac{\cos(qR)}{(qR)^2} \right] = 3N \frac{j_1(qR)}{qR} \, , \tag{4}$$

where $j_1(qR)$ is the spherical Bessel function of the first order and N is the number of atoms in the cluster [48]. The simplest approximation for the description of *a fullerene* is to assume that carbon atoms are uniformly distributed on the surface of a sphere of the radius R. In this case, one derives

$$n(q) = N\,\frac{\sin(qR)}{qR}\ . \tag{5}$$

This form-factor oscillates with the period $q = 2\pi/R \ll 1$. These oscillations form the diffraction pattern of the differential cross section (1) which possesses a series of diffraction maxima and minima whose positions are mainly determined by the radius of the target.

Figure 1 presents the dependence of the cross section $\mathrm{d}\sigma/\mathrm{d}\Omega_{\mathbf{p}_2}$ on the scattering angle θ for elastic collision of a 809-eV electron with the C_{60} fullerene [51]. The figure shows that the cross section possesses a series of diffraction maxima and minima. Experimental data points obtained in Ref. [51] in the two sets of measurements are illustrated by open and closed circles. The cross section dependence obtained theoretically is shown by a solid curve. Experimental data have been normalized to the theoretical cross section at the second diffraction maximum ($\theta = 5°$). Figure 1 shows quite a good agreement of the experimental and the theoretical results in position of the first and the second maxima. The entire pattern of the differential cross section obtained theoretically is very similar to that measured in experiment.

In the vicinity of the diffraction maxima at $\theta < 10°$ the cross section greatly exceeds the elastic scattering cross section on the equivalent number of isolated atoms because of the coherent interaction of the projectile electron with the fullerene sphere.

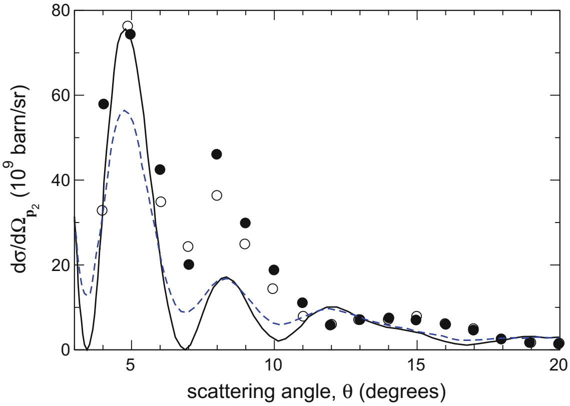

Fig. 1 Experimental (*symbols*) and theoretical (*solid curve*) angular dependencies of the differential elastic scattering cross section in collision of a 809 eV electron with the C_{60} molecule. Symbols correspond to the two independent sets of measurements. *Dashed curve* is the cross section for the mixture containing 60 % of C_{60} and 40 % of equivalent isolated carbon atoms. The figure is adapted from Ref. [51] with editorial modifications

In the region $\theta > 10^\circ$, where $q > 1$, the projectile electron scatters on individual carbon atoms of the fullerene rather than on the entire molecule. Therefore diffraction features of the cross section in the region $\theta < 10^\circ$ are much more pronounced than in the region $\theta > 10^\circ$.

In the region $\theta < 10^\circ$, where $q < 1$, the theoretical cross section has zeros while the experimental one does not. The presence of zeros at $q \approx \pi k/R < 1$ where k is integer, in the theoretical curve is the consequence of the coherent scattering of electron on the fullerene sphere.[1] However, in experiment, zeros in the cross section can disappear because of the presence of carbon atoms or some other impurities in the gas cell. Figure 1 also shows the differential cross section for the mixture containing 60 % of C_{60} and 40 % of isolated carbon atoms (the dashed curve). The differential electron elastic scattering cross section on single carbon atoms does not have diffraction oscillations and thus it forms the smooth background removing zeroes in the angular dependence of the cross section.

3.2 Inelastic Scattering of Electrons on Atomic Clusters

Plasmon excitations in metal clusters and fullerenes have been intensively studied during the past several decades, see, e.g., Refs. [40, 59–66]. They were observed in photoabsorption experiments with metal clusters [42, 43] and in photoionization studies with fullerenes [44, 67–70].

In the photoionization experiments, only the dipole plasmon excitation mode (the angular momentum $l = 1$) can be effectively probed [71, 72]. Electron collective modes with higher angular momenta can be studied in the fast electron–cluster collisions if the scattering angle of the electron is large enough [48–51]. Dipole plasmon resonances of the same physical nature as in the case of the photoabsorption or photoionization dominate the electron energy loss spectrum (EELS) if the scattering angle of the electron, and thus its transferred momentum, is sufficiently small. With increasing scattering angle plasmon excitations with higher angular momenta become more probable. The actual number of multipoles coming into play depends on the cluster size.

In the process of inelastic scattering the projectile electron undergoes the transition from the initial electron state $(\varepsilon_1, \mathbf{p}_1)$ to the final state $(\varepsilon_2, \mathbf{p}_2)$ which is accompanied by the ionization (or, excitation) of a target from the initial state i with the energy ε_i to the final state f with ε_f.

---

[1] In the region $\theta > 10^\circ$, where $q > 1$, the process of elastic scattering on the fullerene shell with the subsequent excitation of surface multipole plasmons becomes dominating. This process is described by the formulas of the second Born approximation which was used to correct the calculated cross section at large values of transferred momentum.

The matrix element, M, which defines the amplitude of the inelastic scattering is given by

$$\begin{aligned} M &= \left\langle f, 2 \left| \sum_a \frac{1}{|\mathbf{r} - \mathbf{r}_a|} \right| 1, i \right\rangle \\ &= \sum_a \int \psi_2^{(-)*}(\mathbf{r}) \psi_f^*(\{\mathbf{r}_a\}) \frac{1}{|\mathbf{r} - \mathbf{r}_a|} \psi_i(\{\mathbf{r}_a\}) \psi_1^{(+)}(\mathbf{r}) \{\mathrm{d}\mathbf{r}_a\} \mathrm{d}\mathbf{r} \,, \end{aligned} \tag{6}$$

where $\{\mathbf{r}_a\} = \mathbf{r}_1 \dots \mathbf{r}_N$ are the position vectors of the delocalized electrons in the target, $\mathbf{r}$ is the position vector of the projectile, $\psi_1^{(+)}(\mathbf{r})$ and $\psi_2^{(-)}(\mathbf{r})$ stand for the initial- and the final state wave functions of the projectile, respectively. Superscripts $(+)$ and $(-)$ indicate that asymptotic behavior of the wave functions is 'plane wave + outgoing spherical wave' and 'plane wave + incoming wave', respectively.

The matrix element can be written as follows:

$$M = \int \frac{4\pi}{q^2} \frac{\mathrm{d}\mathbf{q}}{(2\pi)^3} \left\langle 2 \left| \mathrm{e}^{-\mathrm{i}\mathbf{q}\cdot\mathbf{r}} \right| 1 \right\rangle \left\langle f \left| \sum_a \mathrm{e}^{\mathrm{i}\mathbf{q}\cdot\mathbf{r}_a} \right| i \right\rangle \,, \tag{7}$$

where $\mathbf{q} = \mathbf{p}_1 - \mathbf{p}_2$ is the transferred momentum.

If the velocity of a projectile is high and significantly exceeds the characteristic velocities of delocalized electrons in the target, the first Born approximation is applicable [48]. Within this approximation the initial and the final states of the incident electron can be described by plane waves:

$$\psi_1^{(+)}(\mathbf{r}) = \mathrm{e}^{\mathrm{i}\mathbf{p}_1\cdot\mathbf{r}} \,, \qquad \psi_2^{(-)}(\mathbf{r}) = \mathrm{e}^{\mathrm{i}\mathbf{p}_2\cdot\mathbf{r}} \,. \tag{8}$$

Then, the amplitude of the process reduces to

$$M = \frac{4\pi}{q^2} \left\langle f \left| \sum_a \mathrm{e}^{\mathrm{i}\mathbf{q}\cdot\mathbf{r}_a} \right| i \right\rangle_{\mathbf{q}=\mathbf{p}_1-\mathbf{p}_2} \,. \tag{9}$$

The magnitude q^2 is related to the scattering angle as $q^2 \approx p_1^2\theta^2$ under the assumption that the energy loss $\omega = \varepsilon_1 - \varepsilon_2$ is small, $\omega \ll \varepsilon_1$ (which implies $p_1 \approx p_2$) and the scattering angle is small, $\theta \ll 1$ rad.

Performing the multipole expansion of the exponential factors in (9) (see, e.g., Ref. [73]), one obtains:

$$M = 4\pi \sum_{lm} \mathrm{i}^l \, Y_{lm}^*(\mathbf{q}) \left\langle f \left| \sum_a \phi_l(r_a) Y_{lm}(\mathbf{r}_a) \right| i \right\rangle \,, \tag{10}$$

where the notation

$$\phi_l(r) = 4\pi \frac{j_l(qr)}{q^2} \tag{11}$$

is introduced and j_l is a spherical Bessel function of the order l.

Let us consider a general expression for the cross section of the scattering process:

$$\mathrm{d}\sigma = \frac{2\pi}{p_1}\, \delta(\omega_{fi} - \omega) \sum_{\mathrm{pol}_f} \overline{\sum_{\mathrm{pol}_i}} |M|^2 \,\frac{\mathrm{d}\mathbf{p}_2}{(2\pi)^3}\, \mathrm{d}\rho_f \ . \tag{12}$$

Here $\omega_{fi} = \varepsilon_f - \varepsilon_i$, the sign $\sum_{\mathrm{pol}_f}$ denotes the summation over the projection of the final state f orbital momentum, whereas $\overline{\sum}_{\mathrm{pol}_i}$ denotes the averaging over the projections of the initial state orbital momentum, and $\mathrm{d}\rho_f$ is the density of final states of the target.

Substituting the scattering amplitude (10) into Eq. (12), one derives the doubly differential cross section:

$$\frac{\mathrm{d}^2\sigma}{\mathrm{d}\varepsilon_2 \mathrm{d}\Omega_{\mathbf{p}_2}} = \frac{1}{\pi}\frac{p_2}{p_1} \sum_{lm} \int \left| \left\langle f \left| \sum_a V_{lm}(\mathbf{r}_a) \right| i \right\rangle \right|^2 \delta(\omega_{fi} - \omega)\, \mathrm{d}\rho_f \ , \tag{13}$$

where

$$V_{lm}(\mathbf{r}) = \phi_l(r) Y_{lm}(\mathbf{r}) \tag{14}$$

is the multipolar potential of the fast projectile, $\mathrm{d}\Omega_{\mathbf{p}_2}$ denotes the differentiation over the solid angle of the scattered electron and sign $\int \mathrm{d}\rho_f$ means the summation over the final states (which includes the summation over the discrete spectrum and the integration over the continuous spectrum).

3.3 Plasmon Resonance Approximation

An effective tool for evaluation of the contribution of plasmon excitations to the excitation and ionization spectra of different atomic clusters and NPs is based on the plasmon resonance approximation (PRA) [48, 50, 55, 72]. This approach postulates that the dominating contribution to the cross section in the vicinity of the plasmon resonance frequency comes from collective electron excitations, while single-particle effects give a much smaller contribution. Hence, one can neglect single-particle excitations when calculating the matrix element in Eqs. (12) and (13). During the past decades, this approach has provided a clear physical explanation of the resonant-like structures in photoionization spectra [55, 57, 74] and differential inelastic scattering cross sections [48, 50, 53, 54, 74–76] of small metallic clusters and nanoparticles, as well as carbon fullerenes by the photon, electron and ion impact. It was also applied [55, 77–79] to describe the dynamic response of alkali and noble metal clusters in the processes of radiative electron capture, polarization bremsstrahlung, and multiphoton excitation.

According to Kubo linear response theory [48, 80], the integral on the right-hand side of Eq. (13) can be related to the variation of electron density caused by an external electric field, and the following substitution can be performed:

$$\int \left| \left\langle f \left| \sum_a V_{lm}(\mathbf{r}_a) \right| i \right\rangle \right|^2 \delta(\omega_{fi} - \omega) \mathrm{d}\rho_f \ \rightarrow \ \frac{1}{\pi} \mathrm{Im} \int V_{lm}^*(\mathbf{r}) \delta\rho_l(\omega, q; \mathbf{r}) \mathrm{d}\mathbf{r} \ . \quad (15)$$

Here, $\delta\rho_l(\omega, q; \mathbf{r})$ is the density variation due to the exposure of the system to the multipolar potential $V_{lm}(\mathbf{r})$. In a general case, this variation depends on the transferred energy ω, transferred momentum q and the position vector $\mathbf{r}$.

Using (15) in (13), the doubly differential cross section acquires the form

$$\frac{\mathrm{d}^2\sigma}{\mathrm{d}\varepsilon_2 \mathrm{d}\Omega_{\mathbf{p}_2}} = \frac{1}{\pi^2} \frac{p_2}{p_1} \sum_l \mathrm{Im}\Big[I_l(\omega, q) \Big] \ , \quad (16)$$

where

$$I_l(\omega, q) = \sum_m \int V_{lm}^*(\mathbf{r}) \delta\rho_l(\omega, q; \mathbf{r}) \mathrm{d}\mathbf{r} \ . \quad (17)$$

In the general case, an atomic cluster can be considered as a spherically symmetric system where the charge is distributed homogeneously between two concentric spheres. The width of a spherical shell is defined as $\Delta R = R_2 - R_1$ where R_1, R_2 are the inner and the outer radii of the system, respectively. The equilibrium electron density distribution $\rho_0(r)$ is expressed via the number N_e of delocalized electrons and the system's volume V:

$$\rho_0 = \begin{cases} N_e/V & \text{for } R_1 \le r \le R_2 \\ 0 & \text{if otherwise} \ . \end{cases} \quad (18)$$

The volume of the spherical shell reads as

$$V = \frac{4\pi}{3}\left(R_2^3 - R_1^3\right) = \frac{4\pi}{3} R_2^3 \left(1 - \xi^3\right) \ , \quad (19)$$

where $\xi = R_1/R_2 \le 1$ is the ratio of the inner to the outer radii. Such a "jellium"-shell representation has been successfully utilized for the description of plasmon formation in carbon fullerenes [53, 54, 57] and fullerene-like hollow gold clusters (see Ref. [75] and Sect. 4). For such a geometry, the density variation can be written in the following form

$$\delta\rho_l(r) = \delta\rho_l^{(\mathrm{v})}(r) \Theta(r - R_1) \Theta(R_2 - r) + \sigma_l^{(1)} \delta(r - R_1) + \sigma_l^{(2)} \delta(r - R_2) \ , \quad (20)$$

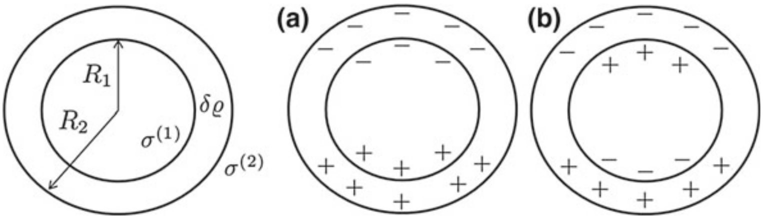

Fig. 2 *Left panel*: Representation of a target system (e.g., a fullerene) as a spherical shell of a width $\Delta R = R_2 - R_1$. Variation of the surface charge densities, $\sigma^{(1,2)}$, and the volume charge density, $\delta\rho^{(\mathrm{v})}$, is also shown. *Right panel*: Representation of the symmetric (**a**) and the antisymmetric (**b**) modes of the surface plasmon. The figure is adapted from Ref. [72] with minor editorial modifications

where $\delta\rho_l^{(\mathrm{v})}(r)$ describes the volume density variation arising inside the shell, and $\sigma_l^{(1,2)}$ are variations of the surface charge densities at the inner and the outer surfaces of the shell, respectively (see the left panel of Fig. 2). In this expression, $\Theta(x)$ and $\delta(x)$ are the Heaviside step function and the delta-function, respectively. The volume density variation causes the formation of the volume plasmon, while the variations of the surface densities correspond to two surface plasmon modes, the so-called symmetric and antisymmetric ones. In the symmetric mode the charge densities of the two surfaces oscillate in phase, while in the antisymmetric mode they are out of phase (see the right panel of Fig. 2). The volume plasmon appears due to compression of the electron density inside the volume of the shell, therefore it does not interfere with either of the surface plasmon modes [72]. The formation of the volume plasmon in the electron impact ionization of metal clusters and carbon fullerenes was revealed in Refs. [52–54]. The model accounting for the contribution of different plasmon modes was successfully utilized to describe the experimentally observed variation of the electron energy loss spectra of C_{60} in collision with fast electrons [53, 54].

The spherical-shell model defined by Eqs. (18) and (19) is applicable for any spherically symmetric system with an arbitrary value of the ratio ξ. Supposing $\xi = 0$ (i.e., $R_1 \to 0$), one obtains a model of a metallic cluster/NP. As a result, the system is treated not as a “jellium” hull but as a full sphere, where the electron density is uniformly distributed inside the sphere of a radius R [49, 52]. In this case, the electron density variation on the surface and in the volume of the cluster or NP leads to the formation of the surface (symmetric mode) and the volume plasmon, respectively, while the antisymmetric surface plasmon mode does not contribute to the cross section. A detailed explanation of this phenomenon can be found in Ref. [72].

Presenting the multipole variation of the electron density, $\delta\rho_l(\omega, q; \mathbf{r})$, as a sum of three contributions (see Eq. (20)), using the explicit expression for the multipolar potential $V_{lm}(r)$ (see Eqs. (11) and (14)), and performing some algebraic transformations, one comes to the formula for the differential inelastic scattering cross section with no damping of plasmon oscillations [72]:

$$\frac{\mathrm{d}^2\sigma}{\mathrm{d}\varepsilon_2\mathrm{d}\Omega_{\mathbf{p}_2}} = \frac{2}{\pi}\frac{R_2}{q^4}\frac{p_2}{p_1}\mathrm{Im}\sum_l\left[\frac{\omega_p^2\,V_l(q)}{\omega^2-\omega_p^2}+\frac{\omega_{1l}^2\,S_{1l}(q)}{\omega^2-\omega_{1l}^2}+\frac{\omega_{2l}^2\,S_{2l}(q)}{\omega^2-\omega_{2l}^2}\right]. \tag{21}$$

In this expression, ω_p is the volume plasmon frequency associated with the ground-state electron density ρ_0 of N_e electrons,

$$\omega_\mathrm{p} = \sqrt{4\pi\rho_0} = \sqrt{\frac{3N_\mathrm{e}}{R_2^3-R_1^3}}\,, \tag{22}$$

and ω_{1l}, ω_{2l} are the frequencies of the two surface plasmon modes of multipolarity l:

$$\omega_{jl} = \left(1\mp\frac{1}{2l+1}\sqrt{1+4l(l+1)\xi^{2l+1}}\right)^{1/2}\frac{\omega_p}{\sqrt{2}}\,,\quad (j=1,2) \tag{23}$$

where '$-$' and '$+$' stand for the symmetric ($j=1$) and antisymmetric ($j=2$) mode, respectively. The volume plasmon frequency, ω_p, is independent of l as it follows from Eq. (22). Functions $V_l(q)$, $S_{1l}(q)$ and $S_{2l}(q)$ are the diffraction factors depending on the transferred momentum q. They determine the relative significance of the multipole plasmon modes in various ranges of the projectile's scattering angles. The dominant contribution of different multipole modes results in a significant angular dependence for the differential electron energy loss spectrum [54]. Explicit expressions for these functions are given in Ref. [72].

Plasmons decay from the collective excitation mode to the incoherent sum of single-electron excitations; therefore, it is essential to account for the damping of plasmon oscillations. This can be done by introducing the finite widths, $\Gamma_l^{(\mathrm{v})}$ and $\Gamma_{jl}^{(\mathrm{s})}$ ($j=1,2$) of the volume and surface plasmon resonances, respectively, and making the following substitutions in the right-hand side of Eq. (21):

$$\begin{aligned}\frac{1}{\omega^2-\omega_{jl}^2} &\to \frac{1}{\omega^2-\omega_{jl}^2+\mathrm{i}\omega\Gamma_{jl}^{(\mathrm{s})}}\,,\\ \frac{1}{\omega^2-\omega_\mathrm{p}^2} &\to \frac{1}{\omega^2-\omega_\mathrm{p}^2+\mathrm{i}\omega\Gamma_l^{(\mathrm{v})}}\,.\end{aligned} \tag{24}$$

The final formula for the differential inelastic scattering cross section which accounts for three plasmons and with damping included is:

$$\frac{\mathrm{d}^2\sigma}{\mathrm{d}\varepsilon_2\mathrm{d}\Omega_{\mathbf{p}_2}} = \frac{\mathrm{d}^2\sigma^{(\mathrm{v})}}{\mathrm{d}\varepsilon_2\mathrm{d}\Omega_{\mathbf{p}_2}}+\frac{\mathrm{d}^2\sigma^{(\mathrm{s}_1)}}{\mathrm{d}\varepsilon_2\mathrm{d}\Omega_{\mathbf{p}_2}}+\frac{\mathrm{d}^2\sigma^{(\mathrm{s}_2)}}{\mathrm{d}\varepsilon_2\mathrm{d}\Omega_{\mathbf{p}_2}}\,, \tag{25}$$

where

$$
\begin{aligned}
\frac{\mathrm{d}^2\sigma^{(\mathrm{v})}}{\mathrm{d}\varepsilon_2 \mathrm{d}\Omega_{\mathbf{p}_2}} &= \frac{2R_2 p_2}{\pi q^4 p_1}\, \omega \sum_l \frac{\omega_\mathrm{p}^2\, \Gamma_l^{(\mathrm{v})}\, V_l(q)}{\left(\omega^2-\omega_\mathrm{p}^2\right)^2 + \omega^2\left(\Gamma_l^{(\mathrm{v})}\right)^2} \\
\frac{\mathrm{d}^2\sigma^{(\mathrm{s}_1)}}{\mathrm{d}\varepsilon_2 \mathrm{d}\Omega_{\mathbf{p}_2}} &= \frac{2R_2 p_2}{\pi q^4 p_1}\, \omega \sum_l \frac{\omega_{1l}^2\, \Gamma_{1l}^{(\mathrm{s})}\, S_{1l}(q)}{\left(\omega^2-\omega_{1l}^2\right)^2 + \omega^2\left(\Gamma_{1l}^{(\mathrm{s})}\right)^2} \\
\frac{\mathrm{d}^2\sigma^{(\mathrm{s}_2)}}{\mathrm{d}\varepsilon_2 \mathrm{d}\Omega_{\mathbf{p}_2}} &= \frac{2R_2 p_2}{\pi q^4 p_1}\, \omega \sum_l \frac{\omega_{2l}^2\, \Gamma_{2l}^{(\mathrm{s})}\, S_{2l}(q)}{\left(\omega^2-\omega_{2l}^2\right)^2 + \omega^2\left(\Gamma_{2l}^{(\mathrm{s})}\right)^2}\ .
\end{aligned}
\tag{26}
$$

The cross section $\mathrm{d}^2\sigma/\mathrm{d}\varepsilon_2\mathrm{d}\Omega_{\mathbf{p}_2}$ can also be written in terms of the energy loss $\omega = \varepsilon_1 - \varepsilon_2 \equiv \Delta\varepsilon$ of the incident projectile of energy ε_1. Integration of $\mathrm{d}^2\sigma/\mathrm{d}\Delta\varepsilon\, \mathrm{d}\Omega_{\mathbf{p}_2}$ over the solid angle leads to the single differential cross section:

$$
\frac{\mathrm{d}\sigma}{\mathrm{d}\Delta\varepsilon} = \int \mathrm{d}\Omega_{\mathbf{p}_2} \frac{\mathrm{d}^2\sigma}{\mathrm{d}\Delta\varepsilon\, \mathrm{d}\Omega_{\mathbf{p}_2}} = \frac{2\pi}{p_1 p_2} \int_{q_{\min}}^{q_{\max}} q\, \mathrm{d}q \frac{\mathrm{d}^2\sigma}{\mathrm{d}\Delta\varepsilon\, \mathrm{d}\Omega_{\mathbf{p}_2}}\ . \tag{27}
$$

As follows from the expressions presented above, the PRA relies on a few parameters, which include the oscillator strength of the plasmon excitation, position of the plasmon resonance peak and its width. The choice of these parameters can be justified by comparing the model-based spectra either with experimental data or with the results of more advanced calculations. Note that values of the plasmon width cannot be obtained directly on the basis of the utilized model. A precise calculation of the widths can be performed by analyzing the decay of the collective excitation mode into the incoherent sum of single-electron excitations. This process should be considered within the quantum-mechanical framework [52] and cannot be treated within the classical physics framework, as the PRA does. In Ref. [52], such an analysis was made to obtain the values of the surface and the volume plasmon width for a Na_{40} cluster. This analysis is discussed in the following section.

3.4 Contribution of the Surface and Volume Plasmon Excitations to the formation of Electron Energy Loss Spectra of Metal Clusters

Damping of the plasmon oscillations is related to the decay of the collective electron excitations to the single-particle ones similar to the mechanism of Landau damping in infinite electron gas. Frequencies of the surface plasmon excitations in neutral metal clusters lie in the vicinity of the ionization threshold. For instance, in small sodium clusters, they are below the ionization potential, and single-particle excitations in the vicinity of the surface plasmon resonance have therefore the discrete spectrum. In this case, the width of a surface plasmon excitation caused by the Landau damping should be treated as the width of the distribution of the oscillator strengths in the vicinity of the resonance. The problem of the formation of the surface plasmon resonance widths in clusters was studied in a number of works [52, 81–83].

The resonance frequencies of volume plasmon excitations in metal clusters are typically located above the ionization threshold. This means that the volume plasmon excitations are quasi-stable and have the real channel of the Landau damping leading to the ionization of the cluster [52]. Thus, the process of inelastic scattering in the region of transferred energies above the ionization threshold can be described as follows. The projectile particle induces the oscillations of the electron density in the cluster; in turn, they cause oscillations of the electric field which result in the ionization of the cluster. The similar scenario takes place with damping of the surface plasmon resonances in fullerenes [84], which also decay via the autoionization channel.

The differential cross section of the electron inelastic scattering on metal clusters obtained in the PRA with accounting for both surface and volume excitations [52] reads as:

$$\begin{aligned}\frac{\mathrm{d}^2\sigma}{\mathrm{d}\varepsilon_2\mathrm{d}\Omega_{\mathbf{p}_2}} &= \frac{4Rp_2}{\pi q^4 p_1}\sum_l (2l+1)^2 j_l^2(qR)\frac{\omega_l^2\,\omega\,\Gamma_l^{(\mathrm{s})}}{(\omega^2-\omega_l^2)^2+\omega^2\left(\Gamma_l^{(\mathrm{s})}\right)^2} \\ &+ \frac{2R^3p_2}{\pi q^2 p_1}\sum_l (2l+1)\frac{\omega_{\mathrm{p}}^2\,\omega\,\Gamma_l^{(\mathrm{v})}}{(\omega^2-\,\omega_{\mathrm{p}}{}^2)^2+\omega^2\left(\Gamma_l^{(\mathrm{v})}\right)^2} \\ &\times\left[j_l^2(qR)-j_{l+1}(qR)j_{l-1}(qR)-\frac{2}{qR}j_{l+1}(qR)j_l(qR)\right],\end{aligned} \tag{28}$$

where $\omega_{\mathrm{p}}=\sqrt{3N_{\mathrm{e}}/R^3}$ is the volume plasmon resonance frequency and $\omega_l=\sqrt{l/(2l+1)}\omega_{\mathrm{p}}$ is the frequency of a surface plasmon excitation with the angular momentum l, $\Gamma_l^{(\mathrm{v})}$ and $\Gamma_l^{(\mathrm{s})}$ are the corresponding widths. The cross section (28) is similar to the expression obtained in Ref. [85] for electron scattering on small metal particles by means of classical electrodynamics.

According to Ref. [52], the width of the surface plasmon resonance in the PRA is equal to:

$$\Gamma_l^{(\mathrm{s})}=\frac{4\pi\,\omega_l}{(2l+1)R}\sum_{\nu,\mu}\left|\left\langle\psi_\mu\left|\varphi_l^{(\mathrm{s})}(\mathbf{r})\right|\psi_\nu\right\rangle\right|^2\delta(\omega_l-\varepsilon_\mu+\varepsilon_\nu), \tag{29}$$

where $\varphi_l^{(\mathrm{s})}(\mathbf{r})=\sum_m\left[(r/R)^l\theta(R-r)+(R/r)^{(l+1)}\theta(r-R)\right]Y_{lm}(\mathbf{n})$. Note that the same expression was obtained in earlier studies [81, 82] using other methods. Evaluation of the expression (29) for sufficiently large clusters leads to the well-known result for the Landau damping of the surface plasmon oscillations, $\Gamma_l^{(\mathrm{s})}=3l\,v_{\mathrm{F}}/R$, where v_{F} is the velocity of the cluster electrons on the Fermi surface [82].

In the PRA, one can also determine the autoionization width of the volume plasmon resonance [52], which is equal to:

$$\varGamma_l^{(\mathrm{v})} = \frac{8\pi^2\omega_\mathrm{p}}{q^2R^3}\,\frac{\sum_\nu \int \left|\left\langle \psi_\mu \left| \varphi_l^{(\mathrm{v})}(\mathbf{r}) \right| \psi_\nu \right\rangle\right|^2 \delta(\omega_\mathrm{p} - \varepsilon_\mu + \varepsilon_\nu)\mathrm{d}\mu}{j_l^2(qR) - j_{l+1}(qR)j_{l-1}(qR) - \frac{2}{qR}j_{l+1}(qR)j_l(qR)}\,, \tag{30}$$

where $\varphi_l^{(\mathrm{v})}(\mathbf{r}) = \sum_m \left[j_l(qr) - j_l(qR)(r/R)^l\right]\theta(R-r)Y_{lm}(\mathbf{n})$. The summation is performed over the occupied single-electron states ν and the integration is performed over the electronic states μ of the continuous spectrum.

The projectile particle excites simultaneously numerous modes of the volume plasmon. The sum of the potentials of all the modes gives the resulting potential $\varphi_l^{(\mathrm{v})}(\mathbf{r})$. It is essential that all normal modes of the volume plasmon have the same resonance frequency ω_p, but the excitation probability for these modes depends on the kinematics of collision. This leads to the dependence of the volume plasmon potential $\varphi_l^{(\mathrm{v})}(\mathbf{r})$ upon the transferred momentum. The oscillations of the volume plasmon potential result in the ionization of the cluster, which probability and the volume plasmon resonance width depend on transferred momentum q. However, the numerical analysis [52] showed that the dependence of $\varGamma_l^{(\mathrm{v})}$ on q is rather weak in the region of $q \ll 1$, where collective electron oscillations mainly take place. Therefore, the volume plasmon resonance width with the given l can be approximated by the limiting value following from Eq. (30) at $q = 0$:

$$\varGamma_l^{(\mathrm{v})} = (2l+5)\frac{\pi^2\omega_\mathrm{p}}{R}\sum_\nu \int \left|\left\langle \psi_\mu \left| \varphi_l^{(\mathrm{v})}|_{q=0}(\mathbf{r}) \right| \psi_\nu \right\rangle\right|^2 \delta(\omega_\mathrm{p} - \varepsilon_\mu + \varepsilon_\nu)\mathrm{d}\mu\,. \tag{31}$$

Figure 3 shows the dependence of the autoionization width $\varGamma_l^{(\mathrm{v})}$ on the transferred momentum q for the volume plasmon modes, which provide significant contribution to the EELS. The width of the dipole, quadrupole and octupole volume plasmon resonances has been calculated according to Eq. (30). The transferred momentum q plays the role of the wave vector for the volume plasmon excitations. All three plasmon modes have the similar dependence of $\varGamma_l^{(\mathrm{v})}$ upon q. The width grows slowly in the region of small q and it decreases rapidly at larger q. In the latter region, the probability of volume plasmon excitation by the incoming electron is correspondingly reduced. Note that the wave length of a collective electron oscillation should be larger than the inter-electronic distance in the cluster, i.e. plasmon wave vector should be smaller than the Fermi momentum of cluster electrons. In the region $q < 0.5$, where the latter condition is fulfilled, the dependence of $\varGamma_l^{(\mathrm{v})}$ upon q is rather weak, and the resonance width can be approximated by the following values: $\varGamma_1^{(\mathrm{v})} \simeq 0.5\omega_\mathrm{p}$, $\varGamma_2^{(\mathrm{v})} \simeq 0.3\omega_\mathrm{p}$, and $\varGamma_3^{(\mathrm{v})} \simeq 0.23\omega_\mathrm{p}$. Contrary to surface plasmons, the autoionization width of a volume plasmon decreases with the growth of the angular momentum.

Figure 4 shows the EELS of a sodium Na_{40} cluster in collision with a 50-eV electron at the scattering angle $\theta = 9°$. The figure illustrates the region of transferred

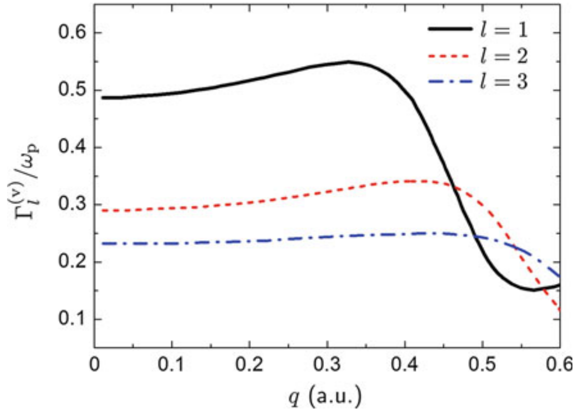

Fig. 3 Autoionization width $\Gamma_l^{(v)}$ of the dipole ($l = 1$), quadrupole ($l = 2$) and the octupole ($l = 3$) volume plasmon excitations as a function of transferred momentum q. The figure is adapted from Ref. [52] with editorial modifications

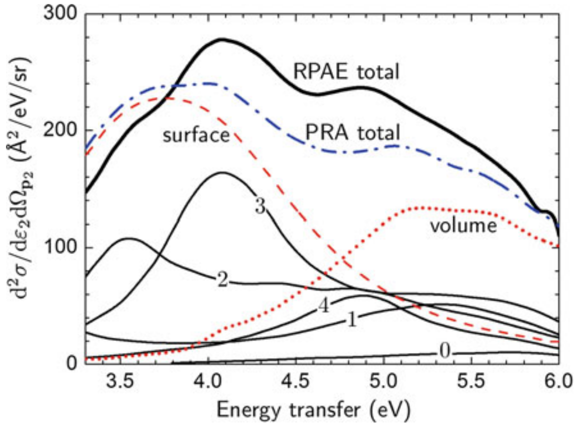

Fig. 4 Differential cross section $d^2\sigma/d\varepsilon_2 d\Omega_{\mathbf{p}_2}$ as a function of the transferred energy ω calculated for the collision of a 50 eV electron with a Na_{40} cluster for the scattering angle $\theta = 9°$ [52]. *Solid lines* represent the RPAE results (see the text for further details). Contributions of the surface and the volume plasmons calculated in the PRA (28) are shown by *dashed* and *dotted lines*, respectively. *Dashed-dotted line* represents the sum of these two contributions

energy above the ionization potential, $\omega > 3.3$ eV, where volume plasmon modes become significant. Solid curves illustrate the spectrum calculated using the random phase approximation with exchange (RPAE) method [49, 71]—an *ab initio* method which takes into account many-electron correlations in a many-particle system. In Fig. 4, the thick curve corresponds to the total EELS calculated with RPAE, while thin curves show various partial contributions corresponding to different angular momenta ($l = 0$ to 4). These curves are marked by numbers. The partial contribution to the EELS with $l < 3$ have the broad maximum in the vicinity of $\omega \simeq 5.1$ eV. Comparison of the EELS calculated within the *ab initio* RPAE approach and the PRA (dash-dotted curve) confirms that idea that the peculiarity in the EELS in the vicinity of $\omega \sim 5$ eV is connected with the volume plasmon excitation. Figure 4 demonstrates that collective excitations provide dominating contribution to the total EELS determining its pattern.

3.5 Polarization Effects in Low-Energy Electron–Cluster Collisions

In the previous section, we have mainly focused on the collisions of fast electrons with metal clusters and fullerenes. When considering low-energy electron–cluster collisions, i.e., when the velocity of the projectile is lower or comparable with characteristic velocities of the delocalized cluster electrons, polarization effects come into play [71]. In Ref. [48], on the basis of the Born theory of electron–cluster collisions, it was shown that electron collisions with metal clusters in the region of collision energies below 3–5 eV should be treated as slow, while for fullerenes, the region extends up to 30 eV.

In the low-energy electron–cluster collisions the role of the cluster polarization and exchange-correlation effects increases dramatically. The polarization potential of electron–cluster interaction sometimes changes completely the qualitative picture of the collision. For instance, this takes place when considering low-energy electron elastic scattering on metal clusters. In this case, the resonant structures can appear in the energy dependence of the electron elastic scattering cross section due to the presence of the bound or quasi-bound states in the system [86, 87].

During the past decades, considerable attention has been devoted, both experimentally and theoretically, to the problem of electron attachment to metal clusters and fullerenes. The electron attachment process is one of the mechanisms which leads to the negative cluster ion formation in gases and plasmas and thus it attracts the interest of numerous researchers. Low-energy electron–fullerene scattering was studied in Refs. [88–91]. For metal clusters, the electron attachment problem has been the subject of the intensive experimental [92–96] and theoretical [77, 97–100] investigations. Below, this problem is discussed in more details.

The very simple picture of attachment is described in many textbooks (see, e.g., Ref. [101]). Let us assume that there exists a Langevin attractive potential of the form

$$V(r) = -\frac{\alpha}{2r^4} \tag{32}$$

outside the cluster radius. The constant α is the static polarizability of the cluster. One can then show that there is an orbiting cross section,

$$\sigma = \left(\frac{2\pi^2\alpha}{\varepsilon}\right)^{1/2}, \tag{33}$$

which sets an upper limit bound to the attachment cross section (the so-called Langevin limit). Here, ε is the kinetic energy of the projectile electron. This simple treatment, if valid, would explain the behavior of the cross section in the vicinity of the threshold.

It is known that metal clusters possess a high polarizability (see, e.g., Ref. [59]); hence, large capture cross sections are anticipated. However, simple attempts to account for attachment by using the static polarizability α are not in accordance with observations [93]. The great weakness of the Langevin model is the treatment of α as an approximate constant. In fact, it possesses a complicated energy dependence due to the dynamical polarizability of the metallic cluster.

The possibility of resonances in the capture cross section was considered theoretically in Refs. [77, 97]. It was demonstrated that low-energy electrons can excite a collective plasmon resonance within the metal cluster in the electron attachment process as a result of a strong dipole deformation of the charge density of the cluster. Later this idea was commented in the context of the measurements performed in Ref. [92], although no clear evidence of the resonant behavior was found. The total inelastic scattering cross sections measured in Ref. [92] included attachment as only one of several possible contributing channels.

The resonant electron attachment mechanism was called in Refs. [77, 97] a “polarizational capture” in analogy with the similar mechanism known in the theory of bremsstrahlung (see, e.g., Ref. [79] and references therein). An important consequence of the polarization mechanism is that the low-energy electron falls into the target and the probability of this process is enhanced. Since the process as a whole is resonant, the enhancement is greatest for energies rather close to the plasmon resonance in the dynamic polarizability of the cluster.

In the attachment process, the electron loses its excess energy. Emission of the photon via the polarizational mechanism, is one of the possible channels of the energy loss [63, 77, 78, 97, 98, 102, 103]. The energy of the electron can also be transferred to the excitations of the ionic background of the cluster [104], which may lead to increase of its vibrations and final fragmentation. In spite of the significant physical difference between various channels of the electron energy loss, they have one important common feature: the energy is transferred to the system via the plasmon excitation. Therefore, calculating the total electron attachment cross section including all possible channels of the electron energy loss in the system, one obtains [98, 99] qualitatively similar dependence of the cross section as it was obtained initially for the radiative channel of electron energy loss [77].

In Ref. [77] the attachment cross section has been calculated within the jellium model in a scheme which holds best if the kinetic energy of the electrons is somewhat higher than the energy of the resonance. Also, it was assumed that the attached ion is created in the ground state. As a useful step in simplifying the calculation, a Kramers-Kronig transformation procedure was introduced to compute the polarizability from the absorption coefficient, thereby circumventing the need for full ab initio calculations. Within this approximate scheme, it was found [77, 97] that the resonant attachment cross section dominates over the non-resonant one by a factor of about 10^3–10^4 near resonance, and is therefore a very significant pathway for electrons of low enough energy.

In Refs. [98, 99], the earlier theoretical work on attachment was extended by including the following improvements: (a) all possible channels of the electron attachment were included and the total cross section of the process was calculated rather than analyzing a particular single channel; no assumption that the system can only return to its ground state had been made; (b) theoretical approximation was used to treat electron energies not only in the resonance region, but also throughout the range of interest; (c) an RPAE calculation of the dynamical polarizability was performed along with the corresponding electron attachment cross sections on the basis of the consistent many-body theory with the use of the Hartree-Fock jellium model wave function; (d) calculations were performed for both neutral and charged cluster targets; (e) the polarization effect on the incoming particle as well as collective excitations of different multipolarity in the target electron system were taken into account; (f) Dyson's equation was used to reduce the problem of the interaction of an extra electron with a many-electron target system to a quasi-single-particle problem in a similar way as it was done for negative atomic ions calculations [105].

An example of such a calculation is shown in Fig. 5a. This plot represents the total and partial electron capture cross sections calculated for neutral potassium K_8 cluster. The inset demonstrates the photoabsorption spectrum of K_8. In Ref. [99] this calculation was performed in various approximations outlined above. It was found that the resonance pattern in the electron capture cross section for the K_8 cluster turns out to be similar in various approaches, although for some other sodium and potassium clusters it is more sensitive to the approximations made [99]. The plasmon resonance in the electron capture cross section is shifted on the value of energy of the attached electron as compared to the photoabsorption case shown in the inset.

Experimental evidence for the resonance enhancement of the cross sections of electron attachment process has been obtained in Ref. [94]. The experimental points from the cited paper are shown in Fig. 5b. Comparison of the two panels of Fig. 5 indicates the reasonable agreement between the predictions of theory and the experimental results. However, more precise measurements would be desirable to resolve the more detailed structures in the electron attachment cross sections.

The plasmon resonance enhanced mechanism of electron attachment considered above is typical for metal clusters rather than for carbon fullerenes. Although fullerenes have many similarities in the properties with metal clusters and also possess the plasmon resonances, the energies of these resonances are much higher ($\sim$7 eV and $\sim$20 eV) and thus cannot be reached at low kinetic energies of the projectile electron.

3.6 Relaxation of Electronic Excitations in Metal Clusters

As described above, the plasmon resonances in metal clusters may lie below the ionization thresholds, i.e., in the region of the discrete spectrum of electron excita-

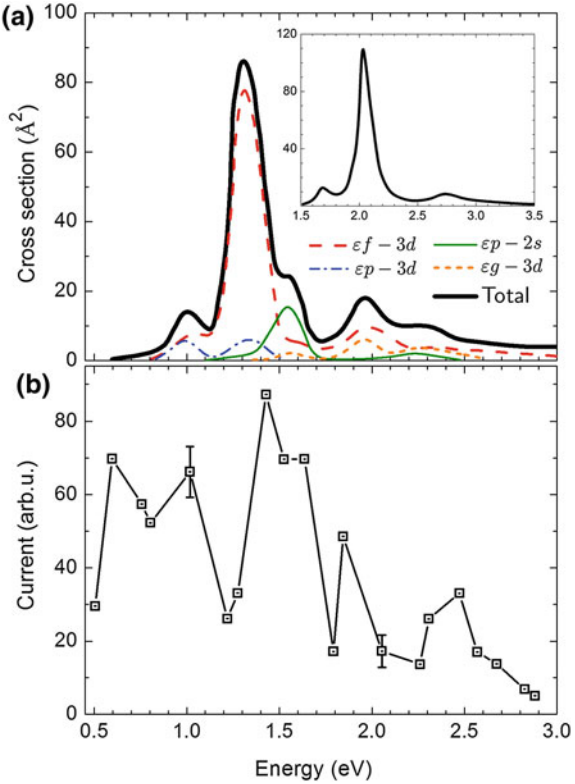

Fig. 5 *Panel a* shows total and partial electron capture cross sections in the vicinity of the plasmon resonance, calculated for a neutral potassium K_8 cluster [99]. The *inset* shows the photoabsorption spectrum of K_8. *Panel b* shows experimental evidence for the resonance enhancement of the electron attachment cross section. The experimental points are from Ref. [94]

tions [61]. This fact rises an interesting physical problem about the eigenwidths of these electronic excitations which possess large oscillator strengths and form the plasmon resonances. Knowledge of these widths is necessary for the complete description of the electron energy loss spectra, electron attachment, polarization bremsstrahlung and photoabsorption cross sections in the vicinity of the plasmon resonances and the description of their dependence on the cluster temperature. The dependence of the plasmon resonance photoabsorption patterns of metal clusters on temperature has been studied experimentally in Ref. [106].

In metal clusters, the origination of the electron excitation widths is mainly connected with the dynamics of the ionic cluster core [104, 107–112]. Let us focus on the influence of the dynamics of ions on the motion of delocalized electrons in metal clusters and discuss it on the basis of the dynamic jellium model suggested in Ref. [107] and developed further in Refs. [104, 113]. This model generalizes the static jellium model [114–116] which treats the ionic background of an atomic cluster as frozen by taking into account vibrations of the ionic background near the equilibrium point. The dynamic jellium model treats simultaneously the vibration modes of the ionic jellium background, the quantized electron motion and the interaction between the electronic and the ionic subsystems. In Ref. [107], the dynamic jellium model was applied for a consistent description of the physical phenomena arising from the oscillatory dynamics of ions.

An important example of the effect, originating from the interaction of the ionic vibrations with delocalized electrons, is the broadening of electron excitation lines. The interest to the problem of the electron excitation linewidths formation in metal clusters was stimulated by numerous experimental data on photoabsorption spectra, most of which were addressed to the region of dipole plasmon resonances [40, 59, 62].

The dynamic jellium model [107] allows one to calculate widths of the electron excitations in metal clusters caused by the dynamics of ions and their temperature dependence accounting for the two mechanisms of the electron excitation line broadening, namely, an *adiabatic* and a *non-adiabatic* (or dynamic) ones.

The *adiabatic* mechanism is connected with the averaging of the electron excitation spectrum over the temperature fluctuations of the ionic background in a cluster. This phenomenon has also been studied in a number of papers [104, 107–112]. The adiabatic linewidth is equal to

$$\varGamma = \sqrt{\frac{4\ln 2}{m\varOmega}\,\mathrm{cth}\left(\frac{\varOmega}{2k_{\mathrm{B}}T}\right)}\,\left|\hat{V}_{\mathrm{nn}}\right| \ . \tag{34}$$

Here m and $\varOmega$ are the mass and frequency corresponding to the generalized oscillatory mode considered, T is the cluster temperature, k_{B} is the Bolzmann constant, and $\left|\hat{V}_{\mathrm{nn}}\right|$ is the matrix element of the electron phonon coupling, calculated for surface and volume cluster vibration modes in Ref. [104].

The mechanism of *non-adiabatic* electron excitation line broadening has been considered for the first time in Refs. [104, 107]. This mechanism originates from the real multiphonon transitions between the excited electron energy levels. Therefore, the dynamic linewidths characterize the real lifetimes of the electronic excitations in a cluster.

According to Ref. [107], the probability of a multiphonon transition from an excited cluster state with electronic and phononic quantum numbers n and N to all possible states (n', N') is equal to

$$\varGamma = \frac{2\pi}{\varOmega}\,|A|^2 = \varOmega\left|\frac{H^2_{\mathrm{n'n}}}{v(q_0)(V_{\mathrm{n'n'}} - V_{\mathrm{nn}})}\right| e^{2(\varphi_{\mathrm{n'}}-\varphi_{\mathrm{n}})} \ . \tag{35}$$

Here $H_{\mathrm{n'n}}$ is the half-distance between the electron energy levels $\varepsilon_{\mathrm{n}}(q)$ and $\varepsilon_{\mathrm{n'}}(q)$ in the tangent point,

$$v(q_0) = \sqrt{\varOmega\left[l^2 - 2S(2N - l - 1) + S^2\right]/2S} \tag{36}$$

is the ion velocity in the tangent point, which is expressed via the number of emitted phonons $l = N' - N$, where N' and N are the phonon numbers, and the parameter

$S = \left| \hat{V}_{\mathrm{nn}} - \hat{V}_{\mathrm{n'n'}} \right|^2 / 2m\Omega^3$; φ_{n}, $\varphi_{\mathrm{n'}}$ are the phases of ionic motion, arising from the distance between the turning points and the tangent point, being equal to

$$\varphi_{\mathrm{n}} = \frac{Z_{\mathrm{n}}\sqrt{Z_{\mathrm{n}}^2 - 2N - 1}}{2} + \frac{2N+1}{4} \ln\left(\frac{Z_{\mathrm{n}} + \sqrt{Z_{\mathrm{n}}^2 - 2N - 1}}{2N+1} \right), \tag{37}$$

where $Z_{\mathrm{n}} = (l - S)/\sqrt{2S}$. The expression for $\varphi_{\mathrm{n'}}$ is the same, but the parameter $Z_{\mathrm{n'}}$ is equal to $Z_{\mathrm{n'}} = (l + S)/\sqrt{2S}$.

The adiabatic broadening mechanism explains the temperature dependence of the photoabsorption spectra in the vicinity of the plasmon resonance via the coupling of the dipole excitations in a cluster with the quadrupole deformation of the cluster surface. The photoabsorption spectra were calculated within the framework of deformed jellium model using either the plasmon pole approximation [108, 109] or the local density approximation [110–112, 117, 118]. In Ref. [112], the octupole deformation of the cluster surface was taken into account. It was demonstrated that the octupole deformation increases the Landau damping as a result of breaking the selection rule, leading to a mixture of the dipole and the quadrupole electronic excitations. Via this mechanism, the octupole deformations of the cluster surface provide the dominating contribution to the thermal broadening of electron excitation lines in small metal clusters.

In Refs. [104, 107] both the adiabatic and non-adiabatic linewidths of electron excitations in the vicinity of the plasmon resonance caused by coupling of electrons with various ionic vibration modes have been calculated. The behavior of the adiabatic and non-adiabatic linewidths as a function of temperature is shown in Fig. 6. The non-adiabatic linewidths characterize the real lifetimes of cluster electron excitations. Naturally, the non-adiabatic widths turn out to be much smaller than the adiabatic ones due to the slow motion of ions in the cluster. However, the adiabatic linewidths do not completely mask the non-adiabatic ones because the two types of widths manifest themselves differently. The adiabatic broadening determines the pattern of the photoabsorption spectrum in the linear regime. The non-adiabatic linewidths are important for the processes, in which the real lifetime of electron excitations and the electron-ion energy transfer are essential. The information about the non-adiabatic electron-phonon interactions in clusters is necessary for the description of electron inelastic scattering on clusters [48–50, 52], including the processes of electron attachment [77, 98, 99], the non-linear photo-absorption and bremsstrahlung [63, 78, 97, 102], the problem of cluster stability and fission. The non-adiabatic linewidths determined by the probability of multiphonon transitions are also essential for the treatment of the relaxation of electronic excitations in clusters and the energy transfer from the excited electrons to ions, which occurs after the impact- or photoexcitation of the cluster.

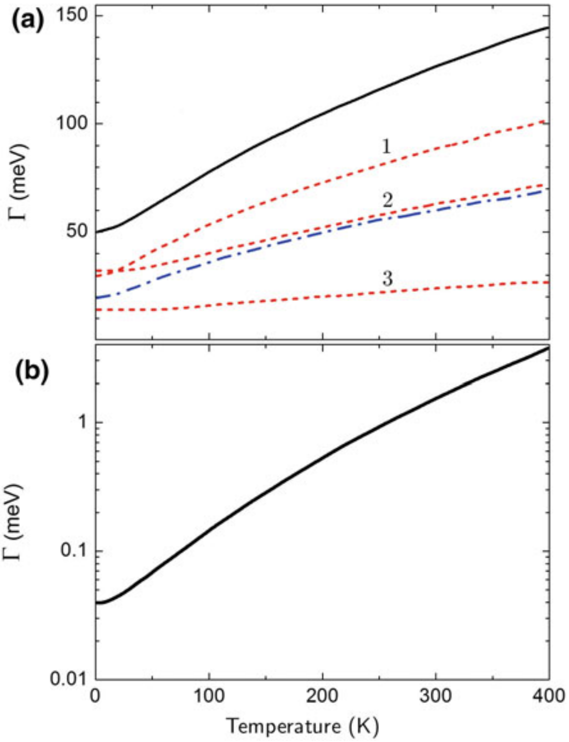

Fig. 6 *Panel a* shows temperature dependence of the adiabatic linewidth Γ, calculated according to (34) for the dipole electron excitation with the energy $\omega_\mathrm{n} = 3.013$ eV in the Na_{40} cluster. *Dashed curves* labeled as 1, 2 and 3 show the adiabatic width corresponding to the electron coupling with the three first volume vibration modes, respectively. *Dashed-dotted curve* shows the adiabatic width arising from the electron coupling with surface vibrations of the cluster. *Solid curve* shows the total adiabatic linewidth. *Panel b* shows temperature dependence of the non-adiabatic width calculated according to Eq. (35) for the dipole excitation with the energy $\omega_\mathrm{n} = 3.013$ eV in the Na_{40} cluster. The figures are adapted from Refs. [104, 107] with minor editorial modifications

In Refs. [104, 107] the role of the volume and the surface vibrations of the ionic cluster core in the formation of the electron excitation linewidths was investigated. It was demonstrated that the volume and surface vibrations provide comparable contributions to the adiabatic linewidths, but the surface vibrations are much more essential for the non-adiabatic multiphonon transitions than the volume ones.

4 Collective Electron Excitations as a Source of Strong Low-Energy Electron Emission from Metal Nanoparticles

As described in the previous section, an important mechanism of ionization or excitation of metallic clusters and NPs, as well as some other nanoscale systems, relies on the formation of plasmons—collective excitations of delocalized valence electrons that are induced by an external electric field [40, 41]. These excitations appear as prominent resonances in the ionization/excitation spectra of various atomic and molecular clusters, and the position of the resonance peak depends strongly on the type of a system. In the case of metallic nanosystems, a typical energy of the plasmon excitations is about several electronvolts, so the resonance peak is located in the vicinity of the ionization threshold [42, 43].

In the recent Monte Carlo simulation [33], the authors included the contribution of plasmon excitations when calculating the spectra of electron emission from metal NPs under proton impact. However, having accounted for the volume plasmon only, they concluded that the plasmon excitation does not play an important role in the process of electron emission, contributing much less to the overall cross sections than individual excitations. On the contrary, the recent studies [74, 75] revealed that a significant increase in the number of emitted electrons due to irradiation of noble metal NPs by fast protons comes from the two distinct types of collective electron effects, namely excitation of delocalized valence electrons in a NP (plasmons) and that of *d* electrons in individual atoms (atomic giant resonances).

The contribution of the plasmon excitations was evaluated by means of the PRA (see Sect. 3.3). In Ref. [75], parameters of the utilized model approach were justified by calculating photoabsorption spectra of several three-dimensional gold clusters. The PRA-based spectra were compared with those obtained by means of a more advanced method, namely by time-dependent density-functional theory (TDDFT) [119]. To evaluate the contribution of individual atomic excitations, an analytical expression was introduced, which relates the cross section of photoionization with that of inelastic scattering in the dipole approximation. In Ref. [74], this methodology was applied for different metal NPs, which have been proposed as sensitizers in radiation therapy applications.

4.1 Collective Electron Excitations in Gold Clusters Under Photon Impact

Figure 7a presents the photoabsorption spectra of the Au_{18}, Au_{20}, Au_{32} and Au_{42} clusters calculated by means of TDDFT for the photon energy up to 60 eV [74, 75]. The spectra, having a similar profile, are characterized by a low-energy peak located below 10 eV and by a broad feature with a maximum at about 25 eV. The analysis performed in Refs. [74, 75] has revealed that the high-energy feature is the atomic

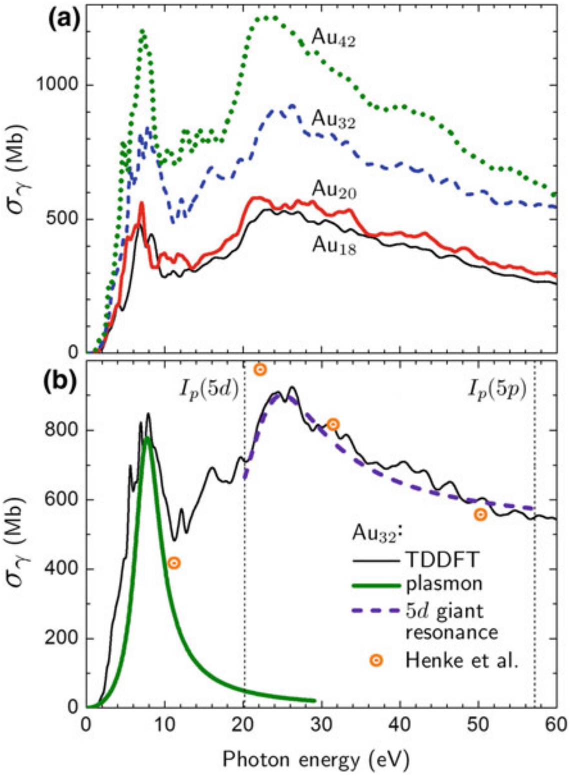

Fig. 7 *Panel a* shows the photoabsorption cross section of the Au$_{18}$, Au$_{20}$, Au$_{32}$ and Au$_{42}$ clusters calculated within the TDDFT framework. *Panel b* shows contribution of the plasmon-type excitation and the 5d giant atomic resonance in the photoabsorption cross section of Au$_{32}$. *Symbols* represent the data for atomic gold [120], multiplied by the number of atoms in the cluster. *Vertical lines* mark the 5d and 5p ionization thresholds in the atom of gold. The figures are adapted from Refs. [74, 75] with minor editorial changes

giant resonance formed due to the excitation of electrons in the 5d atomic shell. The integration of the oscillator strength from 20.2 eV (ionization threshold of the 5d shell in a single atom of gold) up to 57.2 eV (the 5p shell ionization threshold [120]), indicated that about eight localized d-electrons contribute to the excitation of the 5d shell forming the broad peak in the spectrum.

The low-energy peak is due to the plasmon-type excitation, which involves some fraction of s and d electrons delocalized over the whole cluster. The delocalization comes from a partial hybridization of the 6s and 5d atomic shells. Figure 7b shows the TDDFT-based photoabsorption spectrum of a highly-symmetric icosahedral Au$_{32}$ cluster with the diameter of about 0.9 nm (thin solid curve). The results of the calculation are compared to the X-ray absorption data for atomic gold [120], multiplied by the number of atoms in the cluster. The integration of the spectrum of Au$_{32}$ up to 11.2 eV, that is the energy at which the first dip after the resonance peak is observed in the TDDFT spectrum, revealed that about 1.5 electrons from each atom contribute to the collective plasmon-type excitation. On the basis of this analysis, it was stated [74, 75] that the total photoabsorption spectra of gold clusters in the energy region up to 60 eV can be approximated by the sum of the plasmon contribution and that of the 5d electron excitations in individual atoms, $\sigma_\gamma \approx \sigma_{\rm pl} + \sigma_{5d}$.

4.2 Collective Electron Excitations in Small Gold Nanoparticles Under Charge Particle Impact

Similar to the photoionization, the two distinct types of collective electron excitations appear in the process of charge particle impact ionization. The single differential inelastic scattering cross section of a fast projectile in collision with a cluster/NP is then given by

$$\frac{\mathrm{d}\sigma}{\mathrm{d}\Delta\varepsilon} \approx \frac{\mathrm{d}\sigma_{\mathrm{pl}}}{\mathrm{d}\Delta\varepsilon} + \frac{\mathrm{d}\sigma_{\mathrm{at}}}{\mathrm{d}\Delta\varepsilon}\,, \tag{38}$$

where $\Delta\varepsilon = \varepsilon_1 - \varepsilon_2$ is the energy loss of the incident projectile of energy ε_1, $\mathbf{p}_1$ and $\mathbf{p}_2$ are the initial and the final momenta of the projectile, and $\Omega_{\mathbf{p}_2}$ is its solid angle. The cross sections $\mathrm{d}\sigma_{\mathrm{pl}}$ and $\mathrm{d}\sigma_{\mathrm{at}}$ denote the contributions of the plasmon and individual atomic excitations, respectively.

The contribution of the plasmon excitations to the ionization cross section has been described by means of PRA. In this approach, the double differential cross section $\mathrm{d}^2\sigma/\mathrm{d}\Delta\varepsilon\,\mathrm{d}\Omega_{\mathbf{p}_2}$ for a spherical NP is defined as a sum of the surface (s) and the volume (v) plasmon terms, which are constructed as a sum over different multipole contributions corresponding to different values of the angular momentum l (see Sect. 3.3):

$$\begin{aligned}\frac{\mathrm{d}^2\sigma^{(\mathrm{s})}}{\mathrm{d}\Delta\varepsilon\,\mathrm{d}\Omega_{\mathbf{p}_2}} &\propto \sum_l \frac{\omega_l^{(\mathrm{s})2}\,\Gamma_l^{(\mathrm{s})}}{\left(\omega^2-\omega_l^{(\mathrm{s})2}\right)^2+\omega^2\left(\Gamma_l^{(s)}\right)^2}\\ \frac{\mathrm{d}^2\sigma^{(\mathrm{v})}}{\mathrm{d}\Delta\varepsilon\,\mathrm{d}\Omega_{\mathbf{p}_2}} &\propto \sum_l \frac{\omega_{\mathrm{p}}^2\,\Gamma_l^{(\mathrm{v})}}{\left(\omega^2-\omega_{\mathrm{p}}^2\right)^2+\omega^2\left(\Gamma_l^{(\mathrm{v})}\right)^2}\,.\end{aligned} \tag{39}$$

Here $\omega_l^{(\mathrm{s})} = \sqrt{l/(2l+1)}\,\omega_{\mathrm{p}}$ is the frequency of the surface plasmon of the multipolarity l, $\omega_{\mathrm{p}} = \sqrt{3N_{\mathrm{e}}/R^3}$ is the volume plasmon frequency, and the quantities $\Gamma_l^{(i)}$ ($i = \mathrm{s}, \mathrm{v}$) are the corresponding widths. Only the dipole ($l = 1$), quadrupole ($l = 2$) and octupole ($l = 3$) terms were taken into account in this analysis. Excitations with larger l have a single-particle rather than a collective nature [71], thus not contributing to the plasmon formation. The cross sections (39) were obtained within the first Born approximation which is applicable for the collision of a NP with a fast heavy projectile.

As mentioned above, the PRA relies on a few parameters, which include the oscillator strength of the plasmon excitation, position of the peak and its width. In the dipole case, these were validated by fitting the TDDFT-based spectra of several three-dimensional gold clusters to those calculated within the model approach (see Sect. 4.1).

Figure 8a shows the cross section $\mathrm{d}\sigma_{\mathrm{pl}}/\mathrm{d}\Delta\varepsilon$ calculated for a 1 nm gold NP irradiated by fast protons of different incident energies as indicated. The figure demonstrates that the amplitude and the shape of the plasmon resonance depend strongly on the kinetic energy of the projectile. At high velocities, the dipole contribution dom-

Fig. 8 *Panel a* shows contribution of the plasmon excitations to the single differential cross section, $\mathrm{d}\sigma_{\mathrm{pl}}/\mathrm{d}\Delta\varepsilon$, of 1 nm gold NP irradiated by fast protons of different incident energies as a function of the energy loss. *Panel b* shows contribution of different plasmon excitations to the resulting cross section $\mathrm{d}\sigma_{\mathrm{pl}}/\mathrm{d}\Delta\varepsilon$ of a 1 nm gold NP irradiated by a 1 MeV proton

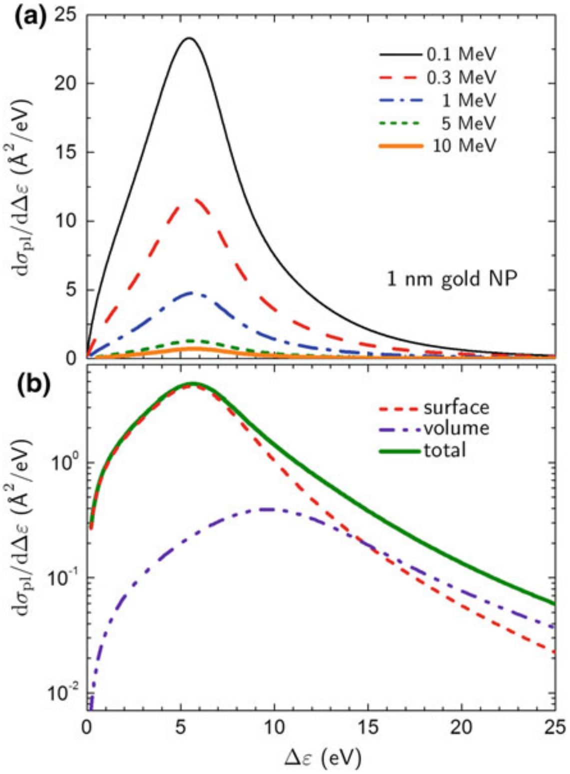

inates over the higher multipole contributions, since the dipole potential decreases slower at large distances than the higher multipole potentials. Figure 8b illustrates the contribution of different plasmon modes to the spectrum of a 1 nm gold NP irradiated by a 1 MeV proton. The main contribution to the cross section in the region of low-energy transfer comes from the surface plasmon, which exceeds that of the volume plasmon by more than an order of magnitude. Thus, the leading mechanism of low-energy electron production by gold NPs is related to the surface plasmon which has not been accounted for in the Monte Carlo simulations [33].

The *d* electrons in the atoms of noble metals play a dominant role at the excitation energies from approximately 20 to 60 eV (see Fig. 7 for the case of gold). For distant collisions, i.e., when the impact parameter exceeds the radius R_{at} of the atomic shell, the ionization spectra of the gold atoms are dominated by the dipole term [58]. Comparison of the cross sections of photoionization, σ_γ, and the dipole term of inelastic scattering, $\mathrm{d}\sigma_{\mathrm{at}}/\mathrm{d}\Delta\varepsilon$, calculated in the Born approximation, leads to the following expression [74, 75]:

$$\frac{\mathrm{d}\sigma_{\mathrm{at}}}{\mathrm{d}\Delta\varepsilon} = \frac{2c}{\pi\omega v_1^2}\sigma_\gamma \ln\left(\frac{v_1}{\omega R}\right), \tag{40}$$

where $\omega = \varepsilon_1 - \varepsilon_2$ is the energy transfer and v_1 is the projectile velocity. Equation (40), obtained within the so-called "logarithmic approximation", assumes that the main contribution to the cross section $\mathrm{d}\sigma_{\mathrm{at}}/\mathrm{d}\Delta\varepsilon$ comes from the region of large distances, $R_{\mathrm{at}} < r < v_1/\omega$. This relation has the logarithmic accuracy which implies that the logarithmic term dominates the cross section while all non-logarithmic terms are neglected [79]. Making an estimate for the gold atoms, it was assumed that $\omega \approx 1$ a.u. which corresponds to the maximum of the $5d$ giant resonance in gold [120], $v_1 \approx 6.3$ a.u. for a 1 MeV proton, and the electron shell radius $R_{5d}(\mathrm{Au}) \approx 2$ a.u. The interaction of the incident projectile with the NP leads to the formation of a giant resonance not in all atoms of the system but only in those located within the impact parameter interval from $r_{\min} \simeq R_{5d}$ to $r_{\max} \simeq v_1/\omega$. This estimate indicates that the $5d$ giant resonance is formed in about one third of atoms of the NP.

To quantify the production of secondary electrons in collision with the NPs, the cross section $\mathrm{d}\sigma/\mathrm{d}\Delta\varepsilon$ (38) is redefined as a function of the kinetic energy E of the electrons: $E = \Delta\varepsilon - I_p$, where I_p is the ionization threshold of the system. The cross section $\mathrm{d}\sigma/\mathrm{d}E$ can be related to the probability to produce N electrons with kinetic energy within the interval $\mathrm{d}E$, emitted from a segment $\mathrm{d}x$ of the trajectory, via [16]:

$$\frac{\mathrm{d}^2 N(E)}{\mathrm{d}x\,\mathrm{d}E} = n\frac{\mathrm{d}\sigma}{\mathrm{d}E}\,, \tag{41}$$

where n is the atomic density of the target.

Figure 9 shows the relative enhancement of the electron yield from a 1 nm gold NP compared to an equivalent volume of pure water. The data for the gold NP have been normalized to the spectrum for liquid water [121]. The dashed line shows the contribution of the plasmon excitations to the electron yield, while the dash-dotted line presents the contribution from the atomic $5d$ giant resonance, estimated using

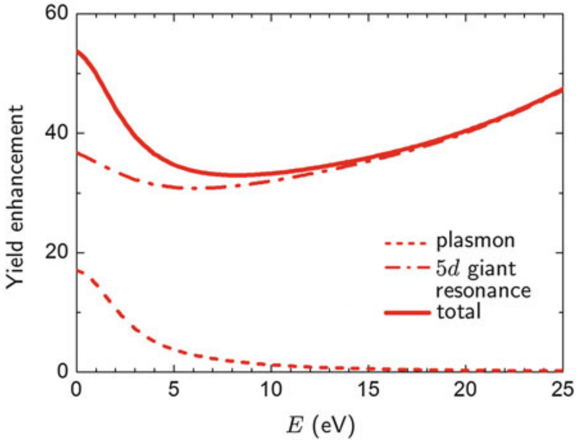

Fig. 9 Electron yield enhancement from the 1 nm gold NP as compared to an equivalent volume of pure water [121]. The *dashed* and *dash-dotted lines* show the contribution of the plasmons and the atomic $5d$ excitations, respectively. *Solid line* illustrates the resulting enhancement

Eq. (40). Making this estimate, we have assumed that the ionization cross sections of individual atoms are dominated by the dipole excitation. Contribution of quadrupole and higher multipole terms will lead to an increase in the number of emitted electrons but their relative contribution will be not as large as that from the dipole excitation. Accounting for the plasmon contribution leads to a significant additional increase in the number of 1–5 eV emitted electrons as compared to the pure water. Due to the collective electron excitations arising in the 1 nm gold NP, it can thus produce up to 50 times larger number of the low-energy electrons comparing to the equivalent volume of pure water medium. The enhancement of the secondary electron yield may increase the number of hydroxyl radicals [15] which recombinate with each other to form more stable hydrogen peroxide H_2O_2 [122]. The latter can propagate for large distances inside the cell and deliver damage to the DNA in the cell nucleus even if the NPs are localized in other cell compartments [25]. Thereby, the results of the analysis performed in Refs. [74, 75] have indicated that the decay of the collective electron excitations in gold NPs is an important mechanism of enhancement of the yield of secondary species. However, more investigation is needed to acquire the complete understanding of all physical and chemical processes involved into the process of radiosensitization due to the NPs.

4.3 Electron Production by Different Metal Nanoparticles

A similar analysis was performed for other metal systems, which are of current interest for cancer treatment with sensitizing NPs. The electron production due to collective electron excitations in small NPs composed of gold, platinum, silver, and gadolinium was analyzed in Ref. [74]. Figure 10 presents the number of electrons per unit length per unit energy produced via the plasmon excitation mechanism by the 1 nm spherical metal NPs due to 1 MeV proton irradiation. Comparative analysis of the spectra demonstrates that the number of low-energy electrons (with the kinetic energy of about a few eV) produced due to the plasmon excitations in the noble metal NPs is about one order of magnitude higher than that by liquid water.

The low electron yield from the gadolinium NP, as compared to the noble metal targets, is explained by the density effects (the atomic density of Gd is about two times smaller than that of the studied noble metals) as well as by the lower plasmon frequency. The maximum of the plasmon resonance peak in the gadolinium NP (4.1 eV) is located below the ionization potential of the system ($\sim$5.0 eV) [123]. In the case of noble metal NPs, the plasmon peak maxima are in the range between 5.5 and 6.0 eV, being in the vicinity of the ionization thresholds. Therefore, the plasmon decay in noble metal NPs results in the more intense electron emission as compared to the gadolinium NP. In the latter case, the plasmon will mostly decay into the single-electron excitations, which can lead to the vibration of the ionic core as a result of the electron-phonon coupling (see Sect. 3.6).

Similar to the case of gold shown in Fig. 9, we have estimated the total number of electrons produced due to the collective excitations in the metal NPs by accounting for

Fig. 10 Number of electrons per unit length per unit energy produced via the plasmon excitations in the 1 nm Au, Pt, Ag and Gd NPs irradiated by a 1 MeV proton. *Dashed curve* represents the number of electron generated from the equivalent volume of water [121]

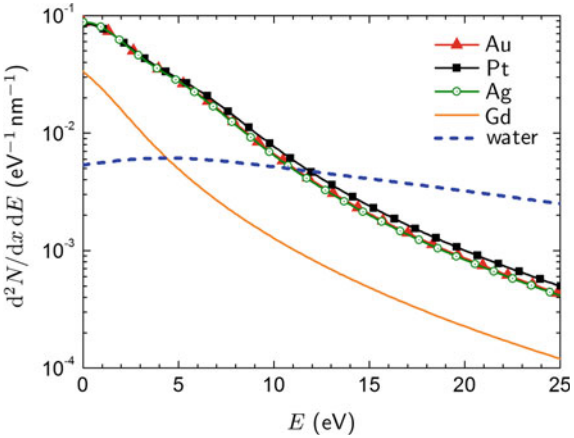

Fig. 11 Yield enhancement from the 1 nm metallic NPs. *Dashed lines* show the contribution of individual atomic excitations. *Solid lines* show the resulting contribution with an account of the plasmons. The figure is adapted from Ref. [74] with minor editorial changes

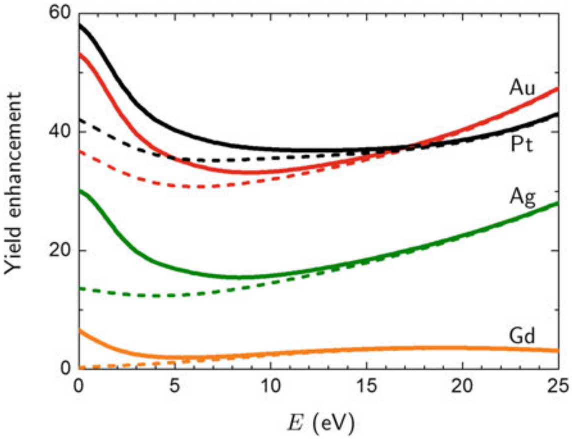

the contribution of excitations in individual atoms. Figure 11 demonstrates the relative enhancement of the electron yield from the considered NPs as compared to pure water. This quantity was obtained by summing up the contribution of the plasmons and individual atomic excitations. Contrary to the noble metals, the Gd atom has a single electron in the 5d shell. Thus, there is no atomic giant resonance in the ionization spectrum of Gd in the 20–60 eV range, and the spectrum is characterized by a narrow peak at $\omega \approx 1.2$ a.u., formed due to ionization of the 5p shell. The dashed lines present the contribution of the atomic giant resonances (5d in Au and Pt, and 4d in Ag) as well as the total $5p + 5d$ contribution in Gd, estimated using Eq. (40). The solid line is the sum of the excitations in individual atoms and the plasmons. The significant yield enhancement arises in those nanoparticles whose constituent atoms possess the giant resonance, contrary to case of gadolinium which has a single 5d electron.

The presented results demonstrate that accounting for the plasmon contribution leads to a significant increase of the 1–10 eV electron yield. For higher electron energies (of a few tens of eV), the main contribution to the electron yield arises from the atomic giant resonance associated with the collective excitation of outer-shell *d* electrons in individual atoms of a NP. As a result of these effects, the number of the low-energy electrons generated by small noble metal NPs (especially, those composed of gold and platinum) significantly exceeds that produced by an equivalent volume of liquid water representing a biological medium.

4.4 Analysis of Different Kinematic Conditions for Charged-Particle Impact

The evolution of the contribution of the plasmon and the giant resonance mechanisms at different kinematic conditions, namely for different projectile velocities and for the NPs of different sizes, was analyzed in Ref. [75]. It was demonstrated that the plasmon contribution to the low-energy (of about 1–10 eV) electron yield from the gold NP can exceed significantly that due to the atomic giant resonance with decreasing the projectile's energy. Indeed, as follows from Eq. (40), at $\varepsilon_1 = 0.1$ MeV ($v_1 = 2.00073$ a.u.), the dipole term of the $5d$ inelastic scattering cross section is strongly suppressed, as the $\ln(v_1/\omega R_{5d})$ term approaches zero. In this case, the yield of electrons with kinetic energy below 5 eV due to the plasmon excitation exceeds that due to the $5d$ atomic excitation by the factor of about 10^3 [75]. This analysis demonstrated that the plasmon mechanism dominates the low-energy electron emission when the incident energy is close to that of an ion in the vicinity of the Bragg peak.

Figure 12 presents the electron yield from the solid gold NPs of different size irradiated by the 1 and 0.1 MeV protons. Metal NPs of this size range were studied recently in relation to the radiotherapies with charged ions [5, 25]. At certain conditions, the contribution of the plasmon excitations saturates, so that larger NPs emit a smaller number of electrons via the plasmon damping mechanism. It was shown previously [48] that the dipole mode of the plasmon excitations arising in a NP gives the dominating contribution to the ionization cross section when the characteristic collision distance exceeds significantly the NP size, $v_1/\omega \gg D/2$, where D is the NP diameter. At large collision distances, the dipole contribution dominates over the higher multipole contributions. Terms with higher l become significant only in the case when the collision distances become comparable with the cluster size. This means that for a given incident energy the plasmon mechanism of electron production will be efficient for relatively small NPs, while the dipole plasmon mode will be suppressed for larger D. A small increase in the number of 5 eV electrons produced by larger NPs as compared to the smaller ones is the result of an increased role of the volume plasmon due to the increased volume/surface ratio. A similar scenario holds for other incident velocities [75].

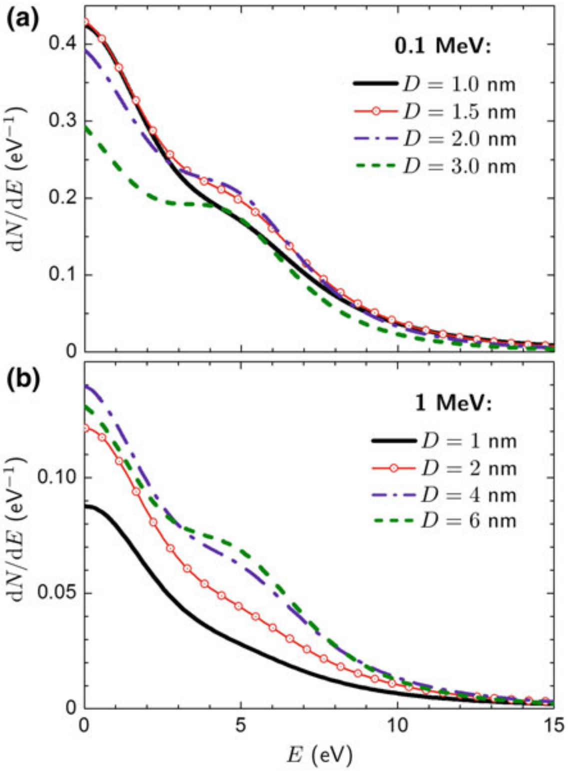

Fig. 12 Number of electrons per unit energy produced via the plasmon excitation mechanism in the solid gold NPs of different size irradiated by the protons of different kinetic energy: 0.1 MeV (**a**) and 1 MeV (**b**). The figures are adapted from [75] with minor editorial changes

5 Enhanced Low-Energy Electron Production by Carbon Nanoparticles

As it was outlined throughout this chapter, excitation of plasmons by an external electric field is a characteristic feature of not only metallic but also, to some extent, of carbon nanoscale systems. For instance, it is well established that plasmon excitations dominate the spectra of photon- and charge-particle impact ionization of fullerenes and polycyclic aromatic hydrocarbons [44, 45, 51, 53, 57, 124, 125].

A recent work [76] presented the spectra of secondary electrons ejected from a carbon NP composed of fullerite, a crystalline form of C_{60} fullerene, irradiated by fast protons. It was demonstrated that the decay of plasmons excited in carbon NPs also enhances the production of low-energy secondary electrons in a biological medium. The contribution of plasmon excitations to the electron production was evaluated by means of the PRA, and the results of these calculations were compared to the model calculations based on the dielectric formalism [121] and Monte Carlo simulations, carried out for pure water medium and for the medium with an embedded NP.

Figure 13 presents the relative enhancement of the electron yield from a 50 nm carbon NP as compared to the equivalent volume of water due to irradiation with

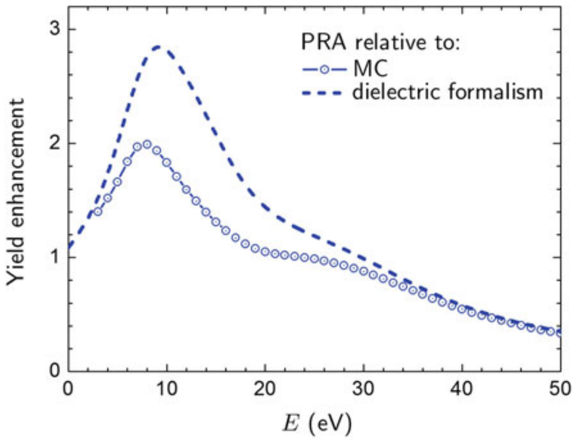

Fig. 13 Electron yield enhancement from the 50 nm carbon nanoparticle as compared to pure water medium. *Dashed line* shows the enhancement due to the plasmon excitations as compared to the results obtained within the dielectric formalism [121]. Open symbols illustrate the plasmon-based enhancement compared to the results of Monte Carlo simulations

1 MeV protons. The enhancement was calculated by comparing the contribution of the plasmon excitations to the electron yield from pure water calculated by means of the dielectric formalism (dashed line) and Monte Carlo simulations (symbols). Depending on the data to be chosen as a reference, the collective electron excitations result in 2–3 times greater number of emitted 10 eV electrons as compared to the case of water. This effect is less pronounced than the enhancement done by small noble metal NPs which can produce up to 15–20 times greater number of electrons via the plasmon decay mechanism as compared to water (see Sect. 4.3). On the other hand, this enhancement results in an excessive emission of the very low-energy electrons of about a few eV, while the carbon-based NP can enhance the yield of more energetic electrons. On this basis, an idea was proposed [76] about considering novel metal-organic sensitizing NPs, where collective excitations will arise in both parts of the system. A proper choice of the constituents may allow for tuning the position of the resonance peaks in the ionization spectra of such systems and, subsequently, for covering a broader kinetic energy spectrum of electrons emitted from such NPs.

6 Conclusions

We presented an overview of theoretical and computational studies of physical phenomena related to the formation and the decay of collective electron excitations in atomic clusters and nanoparticles. These phenomena have a common physical nature and manifest themselves in collision with photons and charged projectiles like electrons, protons or heavier ions. We also made a brief overview of recent Monte Carlo-based studies which have been devoted to the investigation of radiosensitization and dose enhancement effects for proton irradiation combined with metal nanoparticles which are of current interest for radiation therapy applications. Because of a lack of the description of collective electron effects in most of Monte Carlo simulations, many important physical phenomena may be missing. In the presented overview, we emphasized the role of collective electron excitations in various collision processes with atomic clusters and nanoparticles. An accurate description of these phenomena may lead to a better and more complete understanding of the physical picture related to the nanoscale mechanisms of radiation damage in the presence of nanoagents.

Acknowledgements We acknowledge the financial support received from the European Union Seventh Framework Programme (PEOPLE-2013-ITN-ARGENT project) under grant agreement no. 608163.

References

1. Salata OV (2004) Applications of nanoparticles in biology and medicine. J Nanobiotechnol 2:3
2. Murthy SK (2007) Nanoparticles in modern medicine: state of the art and future challenges. Int J Nanomed 2:129–141
3. Herold DM, Das IJ, Stobbe CC, Iyer RV, Chapman JD (2000) Gold microspheres: a selective technique for producing biologically effective dose enhancement. Int J Radiat Biol 76:1357–1364
4. Hainfeld JJ, Slatkin DN, Smilowitz HM (2004) The use of gold nanoparticles to enhance radiotherapy in mice. Phys Med Biol 49:N309–N315
5. Porcel E, Liehn S, Remita H, Usami N, Kobayashi K, Furusawa Y, Le Sech C, Lacombe S (2010) Platimun nanoparticles: a promising material for future cancer therapy? Nanotechnology 21:085103
6. McMahon SJ et al (2011) Biological consequences of nanoscale energy deposition near irradiated heavy atom nanoparticles. Sci Rep 1:8; Corrigendum: ibid. **3**, 1725 (2013)
7. Zhang X-D et al (2015) Ultrasmall glutathione-protected gold nanoclusters as next generation radiotherapy sensitizers with high tumor uptake and high renal clearance. Sci Rep 5:8669
8. McQuaid HN et al (2016) Imaging and radiation effects of gold nanoparticles in tumour cells. Sci Rep 6:19442
9. FP7 Initial Training Network Project “Advanced Radiotherapy, Generated by Exploiting Nanoprocesses and Technologies” (ARGENT), http://www.itn-argent.eu
10. Ali H, van Lier JE (1999) Metal complexes as photo- and radiosensitizers. Chem Rev 99:2379–2450
11. Butterworth KT, McMahon SJ, Currell FJ, Prise KM (2012) Physical basis and biological mechanisms of gold nanoparticle radiosensitization. Nanoscale 4:4830–4838
12. Kobayashi K, Usami N, Porcel E, Lacombe S, Le Sech C (2010) Enhancement of radiation effect by heavy elements. Mutat Res 704:123–131
13. Xiao F, Zheng Y, Cloutier P, He Y, Hunting D, Sanche L (2011) On the role of low-energy electrons in the radiosensitization of DNA by gold nanoparticles. Nanotechnology 22:465101
14. Zheng Y, Hunting DJ, Ayotte P, Sanche L (2008) Radiosensitization of DNA by gold nanoparticles irradiated with high-energy electrons. Radiat Res 169:19–27; Erratum: ibid. **169**, 481–482 (2008)
15. Sicard-Roselli C et al (2014) A new mechanism for hydroxyl radical production in irradiated nanoparticle solutions. Small 10:3338–3346
16. Surdutovich E, Solov’yov AV (2014) Multiscale approach to the physics of radiation damage with ions. Eur Phys J D 68:353
17. Garcia Gomez-Tejedor G, Fuss MC (ed) (2012) Radiation damage in biomolecular systems. Springer Science+Business Media B.V

18. Boudaiffa B, Cloutier P, Hunting D, Huels MA, Sanche L (2000) Resonant formation of DNA strand breaks by low-energy (3 to 20 eV) electrons. Science 287:1658–1660
19. Huels MA, Boudaiffa B, Cloutier P, Hunting D, Sanche L (2003) Single, double, and multiple double strand breaks induced in DNA by 3–100 eV electrons. J Am Chem Soc 125:4467–4477
20. Jain S et al (2011) Cell-specific radiosensitization by gold nanoparticles at megavoltage radiation energies. Int J Radiat Oncol Biol Phys 79:531–539
21. Jain S, Hirst DG, O'Sullivan JM (2012) Gold nanoparticles as novel agents for cancer therapy. Br J Radiol 85:101–113
22. Liu P, Huang Z, Chen Z, Xu R, Wu H, Zang F, Wang C, Gu N (2013) Silver nanoparticles: a novel radiation sensitizer for glioma? Nanoscale 5:11829–11836
23. Luchette M, Korideck H, Makrigiorgos M, Tillement O, Berbeco R (2014) Radiation dose enhancement of gadolinium-based AGuIX nanoparticles on HeLa cells. Nanomed Nanotechnol 10:1751–1755
24. Miladi I et al (2015) Combining ultrasmall gadolinium-based nanoparticles with photon irradiation overcomes radioresistance of head and neck squamous cell carcinoma. Nanomed Nanotechnol 11:247–257
25. Porcel E et al (2014) Gadolinium-based nanoparticles to improve the hadrontherapy performances. Nanomed Nanotechnol 10:1601–1608
26. Kim J-K et al (2010) Therapeutic application of metallic nanoparticles combined with particle-induced X-ray emission effect. Nanotechnology 21:425102
27. Polf JC, Bronk LF, Driessen WHP, Arap W, Pasqualini R, Gillin M (2011) Enhanced relative biological effectiveness of proton radiotherapy in tumor cells with internalized gold nanoparticles. Appl Phys Lett 98:193702
28. Schlathölter T et al (2016) Improving proton therapy by metal-containing nanoparticles: nanoscale insights. Int J Nanomed 11:1549–1556
29. McMahon SJ, Paganetti H, Prise KM (2016) Optimising element choice for nanoparticle radiosensitisers. Nanoscale 8:581–589
30. Sancey L et al (2014) The use of theranostic gadolinium-based nanoprobes to improve radiotherapy efficacy. Br J Radiol 87:20140134
31. Baccarelli I, Gianturco FA, Scifoni E, Solov'yov AV, Surdutovich E (2010) Molecular level assessments of radiation biodamage. Eur Phys J D 60:1–10
32. Schardt D, Elsässer T, Schulz-Ertner D (2010) Heavy-ion tumor therapy: physical and radiobiological benefits. Rev Mod Phys 82:383–425
33. Wälzlein C, Scifoni E, Krämer M, Durante M (2014) Simulations of dose enhancement for heavy atom nanoparticles irradiated by protons. Phys Med Biol 59:1441–1458
34. Lin Y, McMahon SJ, Scarpelli M, Paganetti H, Schuemann J (2014) Comparing gold nanoparticle enhanced radiotherapy with protons, megavoltage photons and kilovoltage photons: a Monte Carlo simulation. Phys Med Biol 59:7675–7689
35. Lin Y, McMahon SJ, Paganetti H, Schuemann J (2015) Biological modeling of gold nanoparticle enhanced radiotherapy for proton therapy. Phys Med Biol 60:4149–4168
36. Martinez-Rovira I, Prezado Y (2015) Evaluation of the local dose enhancement in the combination of proton therapy and nanoparticles. Med Phys 42:6703–6710
37. Krämer M, Kraft G (1994) Calculations of heavy-ion track structure. Radiat Environ Biophys 33:91–109
38. Perl J, Shin J, Schümann J, Faddegon B, Paganetti H (2012) TOPAS: an innovative proton Monte Carlo platform for research and clinical applications. Med Phys 39:6818–6837
39. GEANT4, LEEPWG–Low Energy Electromagnetic Physics Working Group (2013). http://geant4.in2p3.fr/2013/resources/L11-EMLowE.pdf
40. Kreibig U, Vollmer M (1995) Optical properties of metal clusters. Springer, Berlin-Heidelberg
41. Dinh PM, Reinhard P-G, Suraud E (2013) An introduction to cluster science. Wiley, 2013
42. Bréchignac C, Cahuzac Ph, Carlier F, Leygnier J (1989) Collective excitation in closed-shell potassium cluster ions. Chem Phys Lett 164:433–437
43. Selby K, Vollmer M, Masui J, Kresin V, de Heer WA, Knight WD (1989) Surface plasma resonances in free metal clusters. Phys Rev B 40:5417–5427

44. Hertel IV, Steger H, de Vries J, Weisser B, Menzel C, Kamke B, Kamke W (1992) Giant plasmon excitation in free C_{60} and C_{70} molecules studied by photoionization. Phys Rev Lett 68:784–787
45. Ling Y, Lifshitz C (1996) Plasmon excitation in polycyclic aromatic hydrocarbons studied by photoionization. Chem Phys Lett 257:587–591
46. Liebsch T et al (1995) Angle-resolved photoelectron spectroscopy of C_{60}. Phys Rev A 52:457–464
47. Liebsch T et al (1996) Photoelectron spectroscopy of free fullerenes. J Electron Spectrosc Relat Phenom 79:419–422
48. Gerchikov LG, Connerade JP, Solov'yov AV, Greiner W (1997) Scattering of electrons on metal clusters and fullerenes. J Phys B: At Mol Opt Phys 30:4133–4161
49. Gerchikov LG, Ipatov AN, Solov'yov AV (1997) Many-body treatment of electron inelastic scattering on metal clusters. J Phys B: At Mol Opt Phys 30:5939–5959
50. Gerchikov LG, Ipatov AN, Solov'yov AV, Greiner W (1998) Excitation of multipole plasmon resonances in clusters by fast electron impact. J Phys B: At Mol Opt Phys 31:3065–3077
51. Gerchikov LG, Efimov PV, Mikoushkin VM, Solov'yov AV (1998) Diffraction of fast electrons on the fullerene C_{60} molecule. Phys Rev Lett 81:2707–2710
52. Gerchikov LG, Ipatov AN, Polozkov RG, Solov'yov AV (2000) Surface and volume plasmon excitation in electron inelastic scattering on metal clusters. Phys Rev A 62:043201
53. Verkhovtsev AV, Korol AV, Solov'yov AV, Bolognesi P, Ruocco A, Avaldi L (2012) Interplay of the volume and surface plasmons in the electron energy loss spectra of C_{60}. J Phys B: At Mol Opt Phys 45:141002
54. Bolognesi P, Avaldi L, Ruocco A, Verkhovtsev A, Korol AV, Solov'yov AV (2012) Collective excitations in the electron energy loss spectra of C_{60}. Eur Phys J D 66:254
55. Connerade J-P, Solov'yov AV (2002) Formalism for multiphoton plasmon excitation in jellium clusters. Phys Rev A 66:013207
56. Ivanov VK, Kashenock GYu, Polozkov RG, Solov'yov AV (2001) Photoionization cross sections of the fullerenes C_{20} and C_{60} calculated in a simple spherical model. J Phys B: At Mol Opt Phys 34:L669–L677
57. Verkhovtsev AV, Korol AV, Solov'yov AV (2013) Quantum and classical features of the photoionization spectrum of C_{60}. Phys Rev A 88:043201
58. Landau LD, Lifshitz EM (1976) Quantum Mechanics: non-relativistic theory. 3rd edn. Course of Theoretical Physics, vol. 3. Butterworth-Heinemann
59. de Heer WA (1993) The physics of simple metal clusters: experimental aspects and simple models. Rev Mod Phys 65:611–676
60. Brack M (1993) The physics of simple metal clusters: self-consistent jellium model and semiclassical approaches. Rev Mod Phys 65:677–732
61. Bréchignac C, Connerade JP (1994) Giant resonances in free atoms and in clusters. J Phys B: At Mol Opt Phys 27:3795–3828
62. Haberland H (ed) (1994) Clusters of atoms and molecules, theory, experiment and clusters of atoms. Springer Series in Chemical Physics, vol. 52. Springer, Berlin, Heidelberg, New York
63. Korol AV, Solov'yov AV (1997) Polarizational bremsstrahlung of electrons in collisions with atoms and clusters. J Phys B: At Mol Opt Phys 30:1105–1150
64. Alasia F, Broglia RA, Roman HE, Serra L, Colo G, Pacheco JM (1994) Single-particle and collective degrees of freedom in C_{60}. J Phys B: At Mol Opt Phys 27:L643–L650
65. Madjet M, Guet C, Johnson WR (1995) Comparative study of exchange-correlation effects on the electronic and optical properties of alkali-metal clusters. Phys Rev A 51:1327–1339
66. Campbell EE, Rohmund F (2000) Fullerene reactions. Rep Prog Phys 63:1061–1109
67. Berkowitz J (1999) Sum rules and the photoabsorption cross sections of C_{60}. J Chem Phys 111:1446–1453
68. Reinköster A, Korica S, Viefhaus J, Godenhusen K, Schwarzkopf O, Mast M, Becker U (2004) The photoionization and fragmentation of C_{60} in the energy range 26–130 eV. J Phys B: At Mol Opt Phys 37:2135–2144

69. Scully SWJ et al (2005) Photoexcitation of a volume plasmon in C_{60} ions. Phys Rev Lett 94:065503
70. Baral KK et al (2016) Photoionization and photofragmentation of the C_{60}^{+} molecular ion. Phys Rev A 93:033401
71. Solov'yov AV (2005) Plasmon excitations in metal clusters and fullerenes. Int J Mod Phys B 19:4143–4184
72. Verkhovtsev AV, Korol AV, Solov'yov AV (2012) Formalism of collective excitations in fullerenes. Eur Phys J D 66:253
73. Varshalovich DA, Moskalev AN, Khersonskii VK (1988) Quantum theory of angular momentum. World Scientific Publishing, Singapore
74. Verkhovtsev AV, Korol AV, Solov'yov AV (2015) Revealing the mechanism of the low-energy electron yield enhancement from sensitizing nanoparticles. Phys Rev Lett 114:063401
75. Verkhovtsev AV, Korol AV, Solov'yov AV (2015) Electron production by sensitizing gold nanoparticles irradiated by fast ions. J Phys Chem C 119:11000–11013
76. Verkhovtsev A, McKinnon S, de Vera P, Surdutovich E, Guatelli S, Korol AV, Rosenfeld A, Solov'yov AV (2015) Comparative analysis of the secondary electron yield from carbon nanoparticles and pure water medium. Eur Phys J D 69:116
77. Connerade J-P, Solov'yov AV (1996) Radiative electron capture by metallic clusters. J Phys B: At Mol Opt Phys 29:365–375
78. Gerchikov LG, Ipatov AN, Solov'yov AV (1998) Many-body treatment of the photon emission process in electron-clusters collisions. J Phys B: At Mol Opt Phys 31:2331–2341
79. Korol AV, Solov'yov AV (2014) Polarization Bremsstrahlung, Springer Series on Atomic, Optical, and Plasma Physics, vol 80. Springer, Berlin Heidelberg
80. Kubo R (1962) Electronic properties of metallic fine particles. I. J Phys Soc Jpn 17:975–986
81. Lushnikov AA, Simonov AJ (1974) Surface plasmons in small metal particles. Z Phys 270:17–24
82. Yannouleas C, Broglia RA (1992) Landau damping and wall dissipationin large metal clusters. Ann Phys 217:105–141
83. Yannouleas C (1998) Microscopic description of the surface dipole plasmon in large Na_N clusters ($950 \leq N \leq 12050$). Phys Rev B 58:6748–6751
84. Bertsch GF, Bulgac A, Tomanek D, Wang Y (1992) Collective plasmon excitations in C_{60} clusters. Phys Rev Lett 67:2690–2693
85. Lushnikov AA, Simonov AJ (1975) Excitation of surface plasmons in metal particles by fast electrons and x rays. Z Phys B 21:357–362
86. Ipatov AN, Ivanov VK, Agap'ev BD, Eckardt W (1998) Exchange and polarization effects in elastic electron scattering by metallic clusters. J Phys B: At Mol Opt Phys 31:925–934
87. Descourt P, Farine M, Guet C (2000) Many-body approach of electron elastic scattering on sodium clusters. J Phys B: At Mol Opt Phys 33:4565–4574
88. Lezius M, Scheier P, Märk TD (1993) Free electron attachment to C_{60} and C_{70}. Chem Phys Lett 203:232–236
89. Huang J, Carman HS Jr, Compton RN (1995) Low-energy electron attachment to C_{60}. J Phys Chem 99:1719–1726
90. Elhamidi O, Pommier J, Abouaf R (1997) Low-energy electron attachment to fullerenes C_{60} and C_{70} in the gas phase. J Phys B: At Mol Opt Phys 30:4633–4642
91. Ptasinska S et al (2006) Electron attachment to higher fullerenes and to $Sc_3N@C_{80}$. J Phys Chem A 110:8451–8456
92. Kasperovich V, Tikhonov G, Wong K, Brockhaus P, Kresin V (1999) Polarization forces in collisions between low-energy electrons and sodium clusters. Phys Rev A 60:3071–3075
93. Kresin V, Guet C (1999) Long-range polarization interactions of metal clusters. Philos Mag B 79:1401–1411
94. Sentürk S, Connerade JP, Burgess DD, Mason NJ (2000) Enhanced electron capture by metallic clusters. J Phys B: At Mol Opt Phys 33:2763–2774
95. Rabinovitch R, Xia C, Kresin VV (2008) Evaporative attachment of slow electrons to alkali-metal nanoclusters. Phys Rev A 77:063202

96. Rabinovitch R, Hansen K, Kresin VV (2011) Slow electron attachment as a probe of cluster evaporation processes. J Phys Chem A 115:6961–6972
97. Connerade JP, Solov'yov AV (1996) Giant resonances in photon emission spectra of metal clusters. J Phys B: At Mol Opt Phys 29:3529–3547
98. Ipatov A, Connerade J-P, Gerchikov LG, Solov'yov AV (1998) Electron attachement to metallic clusters. J Phys B: At Mol Opt Phys 31:L27–L34
99. Connerade J-P, Gerchikov LG, Ipatov AN, Solov'yov AV (1999) Polarization effects in electron attachement to metallic clusters. J Phys B: At Mol Opt Phys 32:877–894
100. Hervieux P-A, Madjet ME, Benali H (2002) Capture of low-energy electrons by simple closed-shell metal clusters. Phys Rev A 65:023202
101. Massey HSW (1979) Atomic and molecular collisions. Taylor and Francis, London
102. Gerchikov LG, Solov'yov AV (1997) Photon emission in electron-cluster collision in the vicinity of plasmon resonance. Z Phys D 42:279–287
103. Amusia MYa, Korol AV (1994) On the continuous spectrum electromagnetic radiation in electron-fullerene collisions. Phys Lett A 186:230–234
104. Gerchikov LG, Ipatov AN, Solov'yov AV, Greiner W (2000) Non-adiabatic electron-ion coupling in dynamical jellium model for metal clusters. J Phys B: At Mol Opt Phys 33:4905–4926
105. Chernysheva LV, Gribakin GF, Ivanov VK, Kuchiev MYu (1988) Many-body calculation of negative ions using the Dyson equation. J Phys B: At Mol Opt Phys 21:L419–L425
106. Ellert Ch, Schmidt M, Schmitt M, Reiners Th, Haberland H (1995) Temperature dependence of the optical response of small, open shell sodium clusters. Phys Rev Lett 75:1731–1734
107. Gerchikov LG, Solov'yov AV, Greiner W (1999) Dynamical jellium model for metallic clusters. Int J Mod Phys E 8:289–298
108. Pacheco JM, Broglia RA (1989) Effect of surface fluctuations in the line shape of plasma resonances in small metal clusters. Phys Rev Lett 62:1400–1402
109. Bertsch GF, Tomanek D (1989) Thermal line broadening in small metal clusters. Phys Rev B 40:2749–2751
110. Penzar Z, Ekardt W, Rubio A (1990) Temperature effects on the optical absorption of jellium clusters. Phys Rev B 42:5040–5045
111. Montag B, Reinhard P-G, Meyer J (1994) The structure-averaged jellium model for metal clusters. Z Phys D 32:125–136
112. Montag B, Reinhard PG (1995) Width of the plasmon resonance in metal clusters. Phys Rev B 51:14686–14692
113. Lyalin AG, Semenov SK, Cherepkov NA, Solov'yov AV, Greiner W (2000) Hartree-Fock deformed jellium model for metal clusters. J Phys B: At Mol Opt Phys 33:3653–3664
114. Ekardt W (1985) Collective multipole excitations in small metal particles: critical angular momentum l^{cr} for the existence of collective surface modes. Phys Rev B 32:1961–1970
115. Guet C, Johnson WR (1992) Dipole excitations of closed-shell alkali-metal clusters. Phys Rev B 45:11283–11287
116. Kharchenko VA, Ivanov VK, Ipatov AN, Zhizhin ML (1994) Size dependence of electronic structure and adiabatic type of collective vibration in small metal clusters. Phys Rev A 50:1459–1464
117. Wang Y, Lewenkopf C, Tomanek D, Bertsch G, Saito S (1993) Collective electronic excitations and their damping in small alkali clusters. Chem Phys Lett 205:521–528
118. Pacheco JM, Schöne W-D (1997) Shape phase transitions in the absorption spectra of atomic clusters. Phys Rev Lett 79:4986–4989
119. Runge E, Gross EKU (1984) Density-functional theory for time-dependent systems. Phys Rev Lett 52:997–1000
120. Henke BL, Gullikson EM, Davis JC (1993) X-ray interactions: photoabsorption, scattering, transmission, and reflection at $E = 50 - 30,000$ eV, $Z = 1 - 92$. At Data Nucl Data Tables 54:181–342
121. de Vera P, Garcia-Molina R, Abril I, Solov'yov AV (2013) Semiempirical model for the ion impact ionization of complex biological media. Phys Rev Lett 110:148104

122. LaVerne J (1989) Radical and molecular yields in the radiolysis of water with carbon ions. Radiat Phys Chem 34:135–143
123. Yuan HK, Chen H, Tian CL, Kuang AL, Wang JZ (2014) Density functional calculations for structural, electronic, and magnetic properties of gadolinium-oxide clusters. J Chem Phys 140:154308
124. Schüler M, Berakdar J, Pavlyukh Y (2015) Disentangling multipole contributions to collective excitations in fullerenes. Phys Rev A 92:021403(R)
125. Biswas S, Tribedi LC (2015) Plasmon-mediated electron emission from the coronene molecule under fast ion impact. Phys Rev A 92:060701(R)